



Master Photonics for Security Reliability and Safety (PSRS)











COLOR CENTERS IN DIAMOND NEEDLES FOR ALL-OPTICAL SENSING Master Thesis Report

Presented by Elena Filonenko

and defended at
University Jean Monnet

3rd September 2025

Academic Supervisor: Prof. Carlo Ricciardi

Host Supervisors: Dr. Sergei Malykhin and Prof. Polina Kuzhir

Jury Committee:

Prof. Carlo Ricciardi, PoliTo

Prof. Arnaud Meyer, UJM

COLOR CENTERS IN DIAMOND NEEDLES FOR ALL-OPTICAL SENSING

Abstract

This study explores the luminescence properties of color centers in single-crystal diamond needles synthesized via chemical vapor deposition and their potential for alloptical sensing applications. The theoretical part is dedicated to the fundamentals of quantum sensing for different modalities, with the focus on all-optical approaches using diamond color centers. Current achievements and limitations are reviewed, and it is proposed to expand the diamond-based sensing platform by investigating color centers beyond the well-studied NV⁻ and SiV⁻ defects.

The methodological part introduces a pipeline developed in this work for estimating the concentrations of NV charge states through spectral decomposition based on non-negative matrix factorization. Another section addresses the influence of gas composition during chemical vapor deposition growth, specifically the methane content in hydrogen-based mixtures, on the formation and optical properties of color centers. This part results in the identification of methane concentration windows that can be used to control NV charge state incorporation in single-crystal diamond needles.

The experimental part focuses on all-optical thermometry and magnetometry using 389 nm and 468 nm color centers. The results demonstrate the feasibility of these less-explored centers for quantum sensing through characteristic optical signatures, thereby highlighting their potential as promising alternatives or extensions for future diamond-based quantum sensing technologies.

Keywords: quantum sensing, all-optical thermometry, all-optical magnetometry, diamond needles, color centers, photoluminescence, lifetime.

Preface

Apparently, there is nothing easy about being in your early thirties, having already experienced one education and scientific career in your native country, and then deciding to pursue an international master's degree. Although it has been the most crucial and mind-changing experience of my life, the PSRS program also highlighted all my weak spots, sometimes harshly. However, it jump-started immense personal and scientific growth, brought countless opportunities, and introduced me to incredible people, professionals in their fields. For all of this, I am infinitely grateful to the program and to the individuals who lead it and make this life-changing experience possible. My warmest gratitude goes to the PSRS team: Prof. Nathalie Destouches, Amélie Genvrin, Aurore Simonnet, and all other members – for their constant support, countless hours of work, and invaluable help.

To avoid being unfounded about the acquired experience, I want to express my master's thesis journey through some beautiful numbers that mean a lot to me and allow for a more scientific evaluation:

- **1** paper published in a peer-reviewed journal (*Nanotechnology*, IOP Publishing), and another one is currently in preparation;
- **1** Summer School attended on the exciting topic: *New Frontiers in Optical Technologies*;
- 2 Thorlabs grants received for free participation in Optics and Photonics Days one of the most impressive and important scientific events in the Finnish photonics community;
- **3** conference attendances with the presentation of interim scientific results.

Of course, these achievements would have been impossible without my supervisors: Dr. Sergei Malykhin and Prof. Polina Kuzhir – their time, their wise guidance, and their constant support. I first approached Prof. Polina Kuzhir because of my genuine interest in her subject during the second semester of the PSRS program at the University of Eastern Finland. I initially wanted to ask about a lab excursion, but she offered much more by introducing me to Dr. Sergei Malykhin and suggesting I do a mini-research project while at UEF. This is how my deep dive into the world of quantum sensing with color centers in diamond needles began.

I am immensely grateful to Dr. Sergei Malykhin for introducing me to this entirely new scientific field, patiently teaching me how to conduct experiments and interpret results, always bringing new ideas, and being ready to discuss any of my observations. This fruitful collaboration continued during my master's internship, is still ongoing, and I truly hope it will continue into the future.

My thanks also go to my academic supervisor, Prof. Carlo Ricciardi, for his constant support, consultations, and guidance throughout the intricate process of the Master's thesis application and implementation.

Taking everything said into account, I will carry forward this journey not only as a collection of memories and accomplishments, but also as a strong

foundation for my future path in photonics and quantum technologies, thanks to all the people I mentioned in this preface, and to many others who accompanied me throughout the entire duration of the program.

Joensuu, August 2025

Elena Filonenko

Contents

Abstract	iii
Preface	iv
Contents	vi
List of figures	vii
List of tables	x
1 Introduction	1
2 Theoretical Background	4
2.1 Intrinsic properties of diamond and defect formation within its lattice	4
2.2 Controlled engineering of color centers: review of recent studies and curre limitations	
2.3 Basics of quantum sensing, review on sensing principles and notable achievements	11
2.3.1 Spin-based sensing	11
2.3.2 All-optical quantum sensing	12
3 Materials and Methods	15
3.1 Description of SCDNs synthesis	15
3.2 Room-temperature experimental setup	16
3.3 Temperature-controlled experimental setup: cryogenic and physiologically relevant range (25–50 °C)	
3.4 NV ⁻ and NV ^o concentration evaluation	19
3.4.1. Concentration estimation via saturation curve fitting	20
3.4.2 Spectral decomposition via non-negative matrix factorization	21
4 Results and Discussion	26
4.1 General spectral characteristics of synthesized SCDNs	26
4.2 All-optical temperature sensing with 389 nm and 468 nm color centers	31
4.3 All-optical magnetic field sensing with 389 nm and 468 nm color centers	39
4.4 Influence of methane concentration during CVD growth on NV charge state	e 44
Conclusion	48
References	49
Appendix	55
Appendix A. Abbreviations	55
Statement of non-plagiarism	56
Declaration on the use of generative AI tools	57
Supervisor approval	58

List of figures

Figure 1. Diamond cubic structure represented as two FCC lattices intersected and separated from each other along diagonal of the cube by ¼ of its length (Adapted from Viktor Håkansson Ingre, via Wikimedia Commons, licensed under CC BY-SA 4.0 https://creativecommons.org/licenses/by-sa/4.0/)
Figure 2. Diamond types and their corresponding structure (Adapted from "Diamond classification — the diamond types" [PDF], Gemmoraman (2019), https://www.gemmoraman.com/content/uploads/2019/10/DiamondType.pdf)5
Figure 3. Schematic depiction of a) $- NV^0$ and NV^- relative position of energy levels within diamond band gap (adapted from [49]) and b) $- NV^-$ color center energy level structure (adapted from [40])6
Figure 4. Schematic depiction of SiV ⁻ energy level structure (adapted from [43])7
Figure 5. SEM images of a) — grown carbon films containing SCDNs, b) — individual SCDN, c) —. SCDNs after carbon film oxidation and precipitation on silicon plate for further analysis
Figure 6. The schematic representation of FLS1000 Spectrofluorometer (adapted from https://www.edinst.com/products/fls1000-photoluminescence-spectrometer/)16
Figure 7. The schematic representation of temperature-controlled experimental setup.
Figure 8. Typical PL spectrum at 532 nm excitation with NV ⁻ and NV ⁰ ZPLs at 637 nm and 575 nm, respectively, and overlapped PSBs. The ZPLs of NV ⁻ and NV ⁰ centers are marked with black arrows
Figure 9. The NNMF decomposition procedure a) – inputs: NV ⁻ and SiV ⁻ reference curves as seeding shapes and b) – outputs: extracted shapes of three components. 22
Figure 10. Typical PL spectra of the studied samples recorded in the 560–840 nm range without microwave excitation (MW–), with microwave excitation applied (MW+), and the corresponding difference spectrum, which reveals the pure NV^- contribution22
Figure 11. The comparison of decomposition-based NVO shape with etalon CL spectra to evaluate the systematic uncertainty
Figure 12. The decomposition spectrum with a) – back-fitting of the original spectrum (blue) using components for NV^- , NV^0 , and SiV^- derived from NNMF. The numbers above the spectrum are the non-negative least squares scaling coefficients (a, b, c) obtained during the fit, which quantify the contribution strength of each component. b) – the same decomposition after applying a 700/50 nm bandpass filter24
Figure 13. The decomposed spectrum using the 700/50 bandpass filter and the calculated contribution of each component
Figure 14. Power–intensity curves for the mixed NV ⁻ /NV ⁰ emission and for the separated NV ⁻ and NV ⁰ components obtained from their calculated contributions. The

saturation intensity values I _{sat} , extracted from fitting, are indicated in the graph legend.
Figure 15. PL spectra of studied SCDNs obtained under different excitation wavelengths: a), b) – 350 nm; c), d) – 420 nm; e), f) – 530 nm27
Figure 16. Gallery A with all maps plotted using a shared global color scale to facilitate the comparison of the absolute PL intensity between samples
Figure 17. Gallery B with all maps individually normalized to its 95 th percentile intensity to facilitate the assessing of the relative content of specific color centers across the samples
Figure 18. The emission spectra taken at different temperatures (LNT-RT), recording a) – full spectrum of 389 nm center including ZPL and corresponding PSB as well as b) – 389 nm ZPL only. All spectra are normalized by maximum
Figure 19. Temperature dependence of the 389 nm ZPL position and FWHM in the range from LNT to RT. Each uncertainty ribbon includes the corresponding standard deviation of repeated measurements together with the fitting error
Figure 20. The emission spectra taken at different temperatures (LNT-RT), recording a) – 468 nm ZPL and corresponding PSB as well as b) – 468 nm ZPL. All spectra are normalized by maximum
Figure 21. The dependences of 468 nm ZPL position and FWHM value on temperature in the range of LNT-RT
Figure 22. The emission spectra taken at different temperatures (LNT-RT), recording a) – 468 nm ZPL and corresponding PSB, not-normalized, displaying peaks' intensities change and b) – dependence of ZPL intensity to the 3 rd PR intensity ratio on temperature
Figure 23. The recorded for 389 nm color center a) $-$ ZPL at different temperatures (295 $-$ 320 K) as well as b) $-$ the dependences of 389 nm ZPL position and FWHM value on temperature in the range of 295 $-$ 320 K
Figure 24. The recorded for 468 nm color center a) $-$ ZPL at different temperatures (300 $-$ 320 K) as well as b) $-$ the dependences of 468 nm ZPL position and FWHM value on temperature in the range of 300 $-$ 320 K
Figure 25. PL decay curves for the 389 nm color center on a semi-logarithmic scale. 37
Figure 26. PL decay curves for the 468 nm color center on a semi-logarithmic scale. 38
Figure 27. NV ⁻ PL emission spectra recorded in the absence and presence of a magnetic field.
Figure 28. PL emission spectra of the 389 nm color center recorded a) – in the range 385–460 nm and b) – in the range 386–394 nm, in the absence and presence of a magnetic field.
Figure 29. 468 nm PL emission spectra recorded a) — in the range 455-570 nm and b) — in the range 466-473 nm, in the absence and presence of a magnetic field

Figure 30. PL decay curves for the NV ⁻ color center on a semi-logarithmic scale in the absence and presence of a magnetic field41
Figure 31. PL decay curves for a) $-$ 389 nm color center and b) $-$ 468 nm color center on a semi-logarithmic scale in the absence and presence of a magnetic field41
Figure 32. The dependences on methane concentration of a) $-$ NV 0 color center concentration and b) NV $^-$ color center concentration46
Figure 33. NV^- / NV^0 concentrations ratio vs. methane concentration in studied samples47

List of tables

Table 2. Temperature resolutions calculated for different all-optical thermometry methods	Table 1. Gas composition parameters used for PE-CVD growth of SCDNs samples2	26
Table 4. The results of 468 nm color center PL decay curves fitting	· · · · · · · · · · · · · · · · · · ·	34
Table 5. The results of NV color center PL decay curves fitting	Table 3. The results of 389 nm color center PL decay curves fitting	37
Table 6. The results of 389 nm color center PL decay curves fitting	Table 4. The results of 468 nm color center PL decay curves fitting	38
Table 7. The results of 468 nm color center PL decay curves fitting	Table 5. The results of NV ⁻ color center PL decay curves fitting	42
Table 8. Methane concentration for PE-CVD growth of the SCDNs samples	Table 6. The results of 389 nm color center PL decay curves fitting	43
Table 9. Calculation of NV ⁻ concentration from saturation intensities and the resulting values	Table 7. The results of 468 nm color center PL decay curves fitting	43
resulting values	Table 8. Methane concentration for PE-CVD growth of the SCDNs samples	44
		45
		46

1 Introduction

Throughout the whole period of modern technical development, diamond has been playing a pivotal role in numerous applications, such as cutting and drilling tools in heavy industry due to its unrivaled hardness [1,2], thermal management in high-power electronics because of its exceptional thermal conductivity [3,4], and chemically inert coatings for microelectronics, biomedical devices and other applications demanding outstanding chemical stability [5,6].

Using diamonds in a fundamentally new way – specifically in photonics and quantum sensing – started in the second half of the 20th century, when their potential for hosting optically active point defects – color centers – began to be studied [7,8]. The first studies of point defects in natural diamond date back to the 1950s, when nitrogen impurities were identified as major lattice defects [7]. In parallel, the high-pressure high-temperature (HPHT) synthesis of diamonds gained momentum, increasing their availability, while studies confirmed that nitrogen-related centers similar to those in natural diamonds could also be found in these HPHT crystals [9]. Later, with the development of chemical vapor deposition (CVD) techniques in the 1980s, researchers gained even more control over defect incorporation [10]. By that time, it was also feasible to examine point defects' optical and spin properties using photoluminescence (PL) spectroscopy and electron paramagnetic resonance (EPR) [8], thereby laying the foundation for the progress of future diamond-based quantum technologies.

One of the landmark works was issued in 1997, when Gruber *et al.* demonstrated optically detected magnetic resonance (ODMR) at room temperature from a single point defect, containing a nitrogen atom and a vacancy – NV center, and practically launched the direction of diamond-based quantum sensing field [11].

Later, in the early 2000s, optical initialization and coherent manipulation via microwave control of single NV center spins in diamond were successfully demonstrated [12,13]. These advances established NV centers as viable solid-state qubits and laid the foundation for their use in both quantum computing and quantum sensing applications.

In 2008, Balasubramanian et al. in the work [14] demonstrated for the first time that single NV (nitrogen-vacancy) centers in diamond nanocrystals can be used as room-temperature magnetometers, allowing spatial mapping of magnetic fields at the nanoscale.

As the introduction approaches more reliable applications and commercialization, the 2012 article by Maletinsky's group should be mentioned, in which they fabricated the first monolithic all-diamond scanning tip with a single NV center incorporated into a nanopillar – an important step toward practical sensor integration [15].

The first direct mention of diamond as a platform in the context of **all-optical** sensing not relying on microwave driving appears in the work of Sushkov et al. in 2013, where the authors demonstrated the detection of a single-molecule electron spin at room temperature using NV centers [16].

All mentioned research works, as well as many others, led to the

commercialization, patenting, and serial manufacturing of diamond-based devices, and nowadays, several dozen companies are successfully operating in the field of diamond-based quantum technologies, developing quantum sensors, photonic components, and related applications [17–19].

Despite the described progress, state-of-the-art diamond-based quantum technologies such as precise biosensing [20–22], theranostics [23], single-molecule nuclear magnetic resonance (NMR) spectroscopy, external electron spin detection [24], and many others continue to pose challenges in the synthesis of diamond crystals with the required shape, size, color center species and their concentrations, as well as surface properties tailored to specific applications.

One of such challenges is to obtain diamond structures with shapes that enable both precise positioning and individual color center localization, thus allowing for high spatial resolution in sensing and probing applications, or for use as single-photon sources [25].

For these goals, single-crystal diamond needles (SCDNs), grown by CVD, have been recently offered as a promising platform due to their high crystal quality [26] and nanoscale tip curvature [27,28]. A key step toward integrating SCDNs into advanced technologies is a comprehensive understanding of the optical properties of their embedded color centers.

The formation of color centers in diamond as well as their properties are largely influenced by crystal growth conditions, such as gas concentrations, temperatures, substrates etc. and nowadays, many works are dedicated to the problem of color centers engineering [29,30]. The main challenge here lies not only in the large number of variable parameters, but also in the fact that nearly half a thousand different color centers have been identified up to these days in diamond [31], making it difficult to disentangle the specific influence of each condition on the formation and behavior of specific color centers or their combinations. This challenge is also applicable to the synthesis of SCDNs [32–34], and one of the tasks of this study was to investigate how one of the mentioned parameters – gas composition – influences the formation of luminescent color centers in SCDNs. Understanding the influence of gas composition in SCDNs will enable the manipulation of the types, concentrations, and charge states of color centers, advancing precise control over luminescence properties in prospect sensing applications.

A quick review of current scientific research in the field of diamond color centers and their applications shows that the majority of them focus on color centers emitting from the yellow to IR range, with the most studied being NV⁰, NV⁻, and SiV⁻ with zero-phonon lines (ZPL) at 575 nm, 637 nm, and 738 nm, respectively [24,35–40]. The NV⁻ color center exhibits exceptionally long spin coherence times and room-temperature stability, enabling remarkable results in nanoscale magnetometry and biosensing [41,42]. The SiV⁻ color center, in turn, demonstrating the narrow ZPL, short fluorescence lifetime, and great value of optical stability, is also an object of numerous works related to prospects of quantum sensing, photonics circuits, and quantum communication systems [43,44]. There is no doubt that having the instrument allowing to controllably integrate both described color centers into SCDNs' structures would make multifunctional sensing feasible, underlining the relevance and significance of

the present study.

Moreover, to enhance the multifunctionality of SCDN-based quantum sensing platforms, exploring less well-known color centers that emit in the blue-green range [31] is similarly appealing and has been identified as one of the goals of this study. Therefore, the color centers with ZPL at 389 nm and 468 nm, which were also reported to be present in SCDNs [45], were further analyzed regarding their formation depending on different gas composition during SCDN growth and their feasibility for performing various types of quantum sensing using their PL properties.

Therefore, based on the current challenges and state of research described above, this study was aimed at pursuing the following main objectives:

- To investigate how variations in gas composition during CVD growth influence the formation and optical behavior of color centers in SCDNs;
- To identify and study less-explored blue-green-emitting color centers (with ZPL at 389 nm and 468 nm) found in SCDNs, and assess their formation conditions and potential for all-optical sensing applications;

Besides the described tasks, and due to the necessity of analyzing PL spectra of diamond needles containing various overlapping color centers, an additional objective of this study was to develop and implement a signal decomposition algorithm for disentangling the individual contributions of color centers into the overall PL signal.

2 Theoretical Background

2.1 Intrinsic properties of diamond and defect formation within its lattice

As an object of crystallography and materials science, diamond can be characterized by a diamond cubic crystal structure [1]. To simplify the understanding, this structure is often represented by two face-centered cubic (FCC) lattices that intersect and are separated from each other along diagonal of the cube by ¼ of its length (Figure 1). Each carbon atom in such structure forms four sp³ covalent bonds that are, in turn, tetrahedrally arranged.

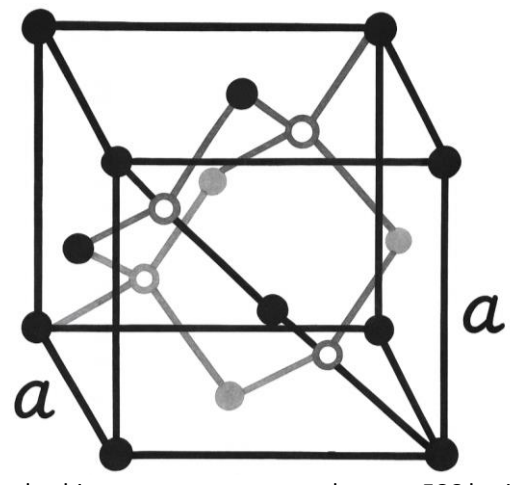


Figure 1. Diamond cubic structure represented as two FCC lattices intersected and separated from each other along diagonal of the cube by ¼ of its length (Adapted from Viktor Håkansson Ingre, via Wikimedia Commons, licensed under CC BY-SA 4.0 https://creativecommons.org/licenses/by-sa/4.0/).

Being a crystal in a real environment, diamond inevitably incorporates impurities, with the most common being nitrogen (carbon-substituting) and boron [46]. One of the widely accepted classifications is based on these impurities content in diamond and represented by the Type I / Type II scheme. The classification is comprehensively reviewed in [31], summarized below, and can be schematically represented in a simplified way by Figure 2.

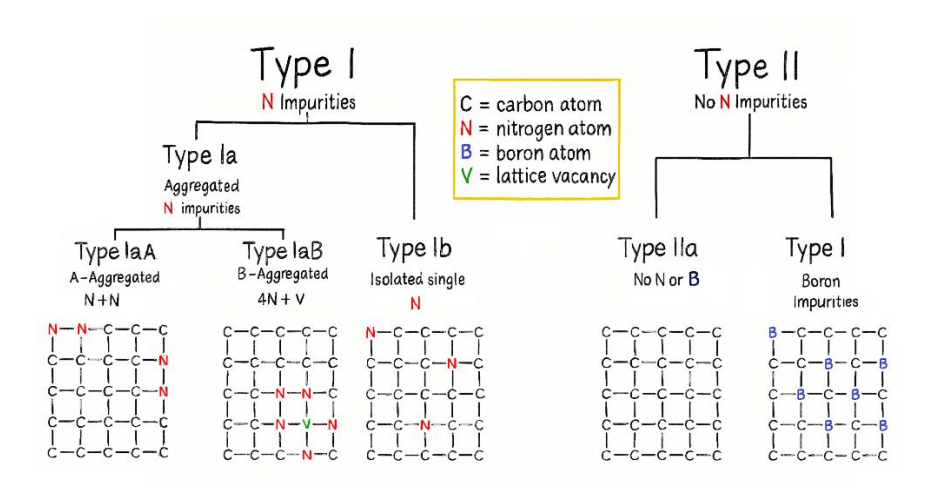


Figure 2. Diamond types and their corresponding structure (Adapted from "Diamond classification – the diamond types" [PDF], Gemmoraman (2019), https://www.gemmoraman.com/content/uploads/2019/10/DiamondType.pdf).

According to this classification, the Type I diamonds group amount to $^{\sim}$ 98 % of natural crystals, the lattice consists of nitrogen-related impurities, whether it is single N atoms, N-pairs or N-vacancy combinations, and can be divided by the way the nitrogen is incorporated into the lattice: Type Ia diamonds are characterized by nitrogen incorporation in aggregates, while Type Ib structure contains single substitutional nitrogen atoms (so-called P1 centers). Only $^{\sim}0.1$ % of natural diamonds can be attributed to this subgroup.

Considering type II, it should be noted, that such structure lacks nitrogen that can be detected, and only 1-2% of natural diamonds fall into this category. The group can be split into two principal sub-groups: Type IIa diamonds - no measurable N, B, or H, and impurity levels are below 10^{17} cm⁻³. These diamonds are of the most optical transparency and electrical insulation. At the same time, the Type IIb structure contains uncompensated boron acceptors making it p-type semiconductor.

From the viewpoint of band theory, diamond is an ultra-wide-band-gap semiconductor, often classified as an insulator, with an indirect band gap of ≈ 5.47 eV at room temperature [31].

Band theory, in turn, is able to further explain diamond's optical behavior: the large gap gives rise to optical transparency from the deep-UV (\approx 225 nm) to the infrared regions [31].

While being transparent in such a wide range, in the presence of defects diamond could possess brought-in optical properties, actively used nowadays in modern diamond photonics. The substitutional impurities, vacancies, or vacancy-impurity complexes introduce discrete electronic states within the diamond band gap, thus producing optically active centers, or so-called color centers. Depending on the form of defects and their energy level structure, color centers' PL properties vary in spectral position of ZPLs, shares of phonon sidebands (PSBs) in total PL, PL decay times, as well as other properties manifested in the PL character and its changes that can be used for quantum sensing.

As was already stated in the introduction, approximately half of the thousand defects [31,47] with their ZPLs, and other traits are known nowadays, and it would be an impossible task to consider all of them in the present study. However, the most studied ones are presented in the work to understand their energy level structure, PL properties, as well as applications and achievements in quantum sensing.

Among the studied color centers, the NV center is the most crucial one [40,48], playing a pivotal role in commercialized diamond-based sensors, and is therefore addressed first in this work. The NV color center is a point defect in the diamond lattice represented by a substitutional nitrogen atom and an adjected lattice vacancy. The nitrogen-vacancy complex exhibits four possible orientations inside the diamond lattice. This complex can bear a neutral (NV⁰) or negative charge (NV⁻) in luminescent states, having different optical properties, respectively. The information on relative positions of NV⁰ and NV⁻ energy levels can be interpreted from Figure 3a, and it is essential for controlling charge state stability, interpreting optical transitions, and further optimization of quantum sensing performance.

In this work, as also in the majority of others, NV⁰ and NV⁻ are considered as two separated color centers, with the NV⁻ being the most crucial one due to its exceptional spin properties, room temperature coherence time of a great value, and the initialization and read out of this color center spin state can be performed optically [40]. These features make it a cornerstone for applications in quantum sensing, including magnetometry, thermometry, and bioimaging [24]. For further understanding of quantum sensing principle with NV⁻ color center, its energy level structure is considered and provided below (Figure 3b).

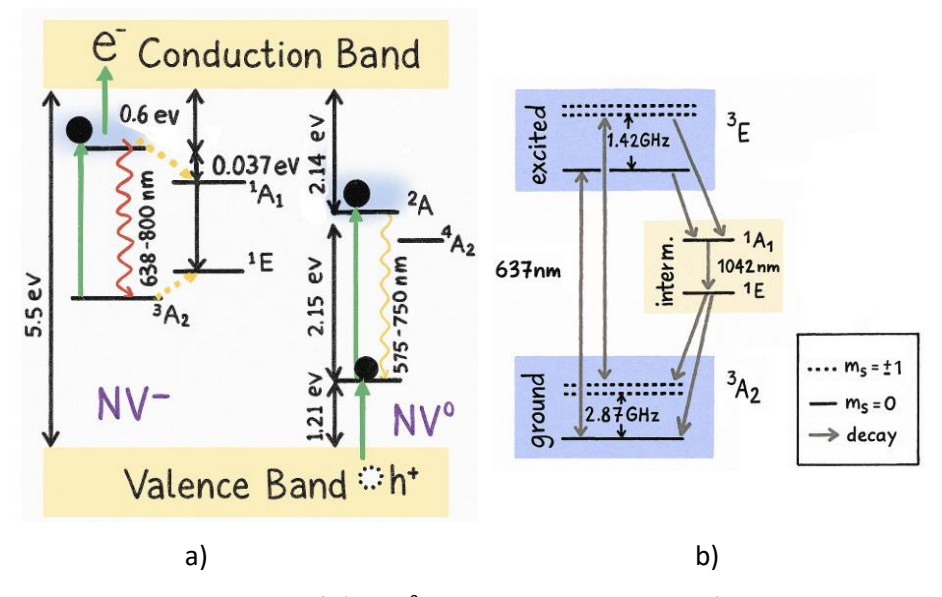


Figure 3. Schematic depiction of a) $- NV^0$ and NV^- relative position of energy levels within diamond band gap (adapted from [49]) and b) $- NV^-$ color center energy level structure (adapted from [40]).

The total number of hosting electrons of NV⁻ system amounts to six, with five electrons being from atoms of nitrogen and adjusted carbons, while the sixth electron

arises from diamond lattice. According to the energy level structure, the NV⁻ center is characterized by triplets on both ground (3 A) and excited states (3 E). These triplets, in turn, contain $m_S = \pm 1$ spin states and $m_S = 0$ spin state. The sublevels are, in turn, split due to zero-field splitting (ZFS) even without an external magnetic field, with typical values of 2.87 GHz and 1.42 GHz at room temperature for ground and excited states correspondingly. In case of $m_S = +1$ and $m_S = -1$ spins are aligned either up or down, respectively, while the $m_S = 0$ case is of antiparallel spins. The structure also contains two intermediate-state singlets (1 A and 1 E) [40]. In the section on Basics of quantum sensing, the principle using the described energy level structure will be discussed in detail.

The next diamond color center to be considered in this work is SiV⁻ color center. The number of publications on its studies has increased rapidly since 2010, with the discoveries that the SiV⁻ center is characterized by a narrow ZPL at 738 nm, a large Debye-Waller factor (0.7) as well as reduced spectral diffusion [50–52]. This combination makes this color center a great instrument in single-photon sources and coherent photonics applications. These qualities with SiV⁻ temperature-dependent intensity are also of service for all-optical thermometry successfully demonstrated in several works [38,43,53].

The SiV⁻ center consists of a silicon atom positioned between two adjacent vacancies, and the complex substitutes two carbon atoms [51].

Figure 4 shows SiV energy level structure as well as relative position of energy levels within the diamond band gap [54,55]. The energy level structure is characterized by ground and excited states being separated by 1.68 eV at room temperature. At cryogenic temperatures, both ground and excited states are represented by orbital doublets, the splitting is due to split spin—orbit interaction and strain [55].

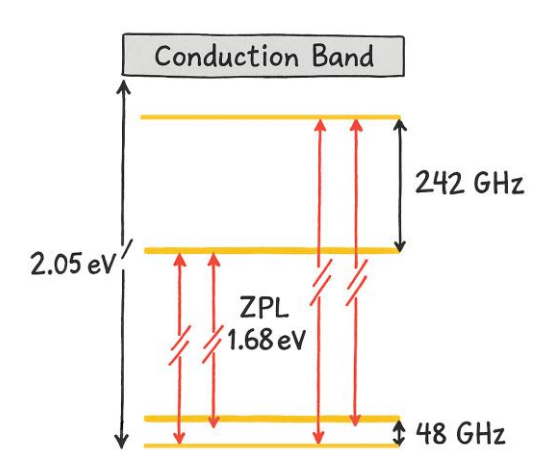


Figure 4. Schematic depiction of SiV⁻ energy level structure (adapted from [43]).

The SiV $^-$ color center, having an additional electron and thus a spin state of S = 1/2, has been studied as the subject of all-optical spin initialization and readout; however, this is possible only at cryogenic temperatures due to extremely fast orbital relaxation and short spin coherence times at room temperature. The appropriate

sensing scheme for this color center will be discussed further in the section on Basics of quantum sensing.

As stated in the introduction, while understanding the behavior of well-known and widely studied NV and SiV centers in SCDN structures is essential, the focus of this study is shifted toward lesser-studied luminescent defects in diamond with ZPLs at 389 nm and 468 nm.

The information about the 389 nm color center is summarized in the work [31] and stating that it is a nitrogen-related defect, appears due to radiation damage of all types of diamonds, and is observed in CVD diamond films. According to work [56], nitrogen can occupy an interstitial position, or, as stated in works [57], nitrogen is substitutional, forming a bond with carbon atoms. The nitrogen, according to work [58], is bonded with interstitial atoms.

The 468 nm color center is, as well, related to the nitrogen defects, being observed in single-crystal CVD diamond of high quality. At the same time, according to work [59], the 468 nm color center is reported to have an association with silicon impurities arising from the CVD growth of diamond on silicon substrates. The latest work [60], however, states that this color center, responsible for the brown color of diamond, is represented by NVH⁻ complex – hydrogen-passivated NV centers.

Recently, density functional theory (DFT) within a dual cubic/lonsdaleite diamond structure calculations in the works [61] demonstrated that the 389 nm and 468 nm centers could be linked to N_3V defects in two different geometrical configurations (C_{1h} and C_{3v} , respectively). Although this approach employs a nonstandard diamond lattice, it enabled the authors to reproduce modelled PL spectra in good agreement with experimental observations. This finding could provide a new theoretical perspective, while challenging the existing experimental interpretations of these color center configurations.

While precise energy-level schemes within the diamond band gap remain undetermined for these color centers, their ZPL emission wavelengths - 389 nm (3.18 eV) and 468 nm (2.65 eV), respectively - place them well within the \sim 5.5 eV band gap of diamond. These traits make them appealing as violet and green light quantum emitters while demanding a comprehensive analysis of their formation mechanisms, PL properties, and sensing potential, especially in SCDNs as a promising sensing platform.

2.2 Controlled engineering of color centers: review of recent studies and current limitations

The ability to form specific color centers while controlling their density, localization, as well as charge state is a critical prerequisite for their integration into quantum sensing devices. Despite substantial progress in this field by the force of numerous research groups, the task of color centers controlled engineering remains a complex challenge, especially as quantum technology demands increasingly precise solutions. It is also worth noting that the vast majority of such works are directed at the formation of NV-color centers, due to their proven applicability in quantum sensing. Therefore, the main goals of these works are not only to ensure the efficient creation of NV-, but also

to suppress the formation of other charge states of NV defects and undesired nitrogenrelated complexes.

In the present work, this challenge is considered in the context of CVD of diamond, since this method stands out as the preferred one for synthesizing SCDNs [62]. Compared to HPHT synthesis or post-growth techniques such as ion implantation, the CVD method allows in situ introduction of dopant gases, such as nitrogen, enabling atomic-scale tuning of color-center formation during growth [28,34]. Moreover, plasma-enhanced CVD (PE-CVD) operates at moderate temperatures (~700–900 °C), minimizing thermal stress and vacancy migration that can hinder localization of centers – a vital property in the context of quantum communication and sensing.

In the PE-CVD process of diamond growth, plasma is generated by direct current, microwave or radio-frequency excitation in a gas mixture containing hydrogen and a carbon source, most commonly methane. The plasma activates the dissociation of methane, allowing carbon radicals to be deposited onto a substrate surface and crystallize into diamonds. Although defect formation is conditioned by many factors, such as choice of substrate, growth temperature, post-growth annealing, as well as ion implantation, the gas composition during growth often has the most direct and reproducible impact [63]. In the following section, recent research on the controlled engineering of color centers is reviewed, with a particular focus on the role of gas composition during CVD synthesis.

The influence of methane concentration during the growth stage has been considered in several works, allowing to understand the common trends. First, in the work [64] dedicated to the growth of thick large-grained polycrystalline diamond films, the authors concluded that the acceptable methane range for high-crystalline diamond phase is limited by 3,75% CH₄ concentration in hydrogen plasma. Authors observed that the increase of methane concentration from 3.75% to 7.5%, although causing the rate of growth to almost triple, leads to the appearance of numerous defects and a non-diamond carbon phase.

In the work [29] titled as "Improving NV centre density during diamond growth by CVD process using N_2O gas" authors modified substrate temperature and methane concentration from 850 °C to 1000 °C and from 3% to 7%, respectively, and reported that lower methane concentrations combined with lower temperatures favors doping and NV^- centers over NV^0 formation.

Authors [65] in their work employed methane concentrations of 0.14%, 1%, and 1.8% to investigate the charge states of NV centers in CVD diamonds doped with nitrogen and phosphorus. Although the authors did not explicitly state their reasoning, it can be inferred that this range of parameters was chosen as optimal, balancing growth rates and defect incorporation while maintaining the crystallinity of structures.

To sum up, although optimal methane concentration windows for efficient diamond growth and defect incorporation can be identified from existing literature and applied to the PE-CVD synthesis of SCDNs, to the best of our knowledge, no systematic investigation has yet been conducted on how varying methane concentrations influence the formation of different color centers.

Another gas that is widely researched in the context of color centers formation during CVD diamond growth is nitrogen. It should be noted that the majority of works

dedicated to the topic of nitrogen content are focusing on NV⁻ centers formation, charge-state control, and they are aiming to increase NV⁻ density while suppressing the neutral NV⁰ state and other nitrogen-related defects.

In one of the fundamental works on NV⁻ formation studying [63], it was reported that rather than the post-growth vacancies migration or components association, NV centers grow as units, and that only a small fraction (less than 0.5%) of nitrogen incorporated during growth is converted into NV centers. This observation led to the conclusion that gas-phase nitrogen availability during the synthesis stage is of the main importance, rather than post-processing nitrogen-related manipulation.

In the work [66], the authors systematically analyzed the effect of varying the N/C ratio in 50 -10⁶ ppm range on the NV⁻ centers formation. From the methane concentrations reported by the authors for this work (ranging from 2.2% to 2.7%), and considering that carbon is sourced from methane, the nitrogen concentration can be estimated to vary from 0.00033% to 2.7%. The authors concluded that the as-grown diamond might contain NV⁻ concentrations ranging from 0.03 to 28.5 ppb, corresponding to the variation in nitrogen content. They concluded that, although increased nitrogen doping leads to higher NV⁻ density, the drawback would be a reduced coherence time – a duration over which the quantum state of an NV⁻ center remains stable and usable for quantum applications. As it was assumed in [67,68] the nitrogen electrons are serving as a decoherence origin, which was also proved in the discussed work, proposing the window for N/C ratio to be in the range from 150 to 8500 ppm or approximately 0.00033% to 0.02295% of nitrogen.

In the work [69] on nitrogen incorporation and NV⁻ centers formation within different conditions for delta-doped CVD-grown diamond layers, the authors reported on high NV⁻ concentration (~0.5 ppm) achieved in the process of growth with a methane concentration equal to $\approx 0.144\%$ and a nitrogen concentration amounted to $\approx 2.06\%$. Authors also conclude that high nitrogen concentrations could lead to a decrease in growth rate, with the saturation condition in their work being equal to 4000 ppm or 0,4% of nitrogen. It should also be mentioned that the study employed a microwave PE-CVD reactor, designed for nanometer-scale delta layer doping with rapid gas flow modulation, allowing abrupt transitions between dopant gas introduction and undoped growth phases. In contrast, common CVD reactors are not equipped with such systems, resulting in less predictable nitrogen incorporation, interfering with the targeted formation of color centers.

As can be seen from this literature review, numerous studies have analyzed the influence of nitrogen content on the formation and charge state of NV centers, and some of them adopt a systematic approach across wide N/C ratios and synthesis conditions. Although nitrogen concentration values reported in these works can be used as reference points for SCDNs growth, the reactor design, gas flow dynamics, and specific growth conditions vary significantly across CVD systems and should be taken into account. Therefore, the exact values and reported trends cannot be transferred directly. Moreover, the goal of this work is not limited to NV center formation, but also extends to analyzing other color centers, whose response to nitrogen doping may differ and requires further investigation.

2.3 Basics of quantum sensing, review on sensing principles and notable achievements

Quantum sensing with color centers of diamond-based platforms is becoming an independent field that, in accordance with how the quantum state of the color center is addressed, manipulated, and read out, can be separated into two main directions:

- Spin-based sensing, relying on microwave (MW) or RF-driven manipulation of spin states [40,70];
- All-optical quantum sensing, which avoids MW or RF application for spin-state manipulation and uses only optical signature dynamics [16,35,71].

Although the present study is focused on the concept of **all-optical quantum sensing**, the principle of spin-based quantum sensing will also be addressed further to outline the advantages and limitations of this approach in comparison with the alloptical one.

2.3.1 Spin-based sensing

As already discussed in the introduction and in the chapter on defect formation within the diamond lattice, the NV⁻ color center is currently the most renowned and widely utilized defect, owing to its well-characterized energy level structure and spin-state properties, which have been successfully implemented in various quantum sensing applications. According to Figure 3b, NV⁻ center is characterized by the ground and excited states being triplet states ($m_5 = 0$ and $m_5 = \pm 1$). Once optically excited with $^{\sim}520-540$ nm from ground ($^{3}A_2$) to excited states (^{3}E), the electron of the system may overcome a radiative decay emitting at 650–750 nm or relax back taking non-radiative path ($^{1}A_1$ / ^{1}E) through intersystem crossing (ISC) finally decaying from there to $m_5 = 0$ of ground state [40].

If the electron is excited while being in the $m_S = 0$ spin sublevel of the ground state, it will most likely avoid the intersystem crossing path, decaying radiatively and contributing fully to the PL signal. Oppositely, excitation from the $m_S = \pm 1$ sublevels leads the electron to preferentially follow the "dark path" (with ~30% probability) via intersystem crossing, resulting in reduced PL intensity [40] (Figure 3b).

This spin-dependent decay behavior makes optically detected magnetic resonance (ODMR) a key technique for NV⁻-based sensing. The method involves three main steps: optical spin initialization, microwave-driven spin manipulation, and optical readout via PL detection.

Firstly, the optical excitation initializes the electron spin into the m_S = 0 state: by irradiation with a green laser, the electron spins go through a cycle, resulting in electron spin polarization – the situation when practically all ground state electron spins are in the m_S = 0 state.

To understand the next step of spin manipulation, it is necessary to consider the NV⁻ ground-state spin Hamiltonian, which can be described as follows [40,70]:

$$H_{gs} = D_{gs} \left[S_z^2 - \frac{S(S+1)}{3} \right] + E_{gs} \left(S_x^2 - S_y^2 \right) + \gamma_e \mathbf{B} \cdot \mathbf{S} + H_{HF}$$
 (1)

In this equation, D_{gs} - longitudinal zero-field splitting (ZFS) equal to 2.87GHz and E_{gs} - transverse ZFS, **S** - the electron spin-1 operator, $S_{x,y,z}$ - spin matrices, γ_e - electron gyromagnetic ratio, S - spin number, **B** - the magnetic field, and H_{HF} stands for the hyperfine interaction term. From the Hamiltonian equation (2.1), the resonance frequencies for transitions between the spin states m_S = 0 and m_S = ±1 could be obtained as follows:

$$\nu_{\pm} = D_{gs} \pm \sqrt{E_{gs}^2 + (\gamma_e B_0)^2}$$
 (2)

In this equation, B_0 is the magnetic field oriented along the NV axis. From this expression, it can be seen that variations in the external magnetic field would result in changes to the ODMR resonance frequencies.

Therefore, for the spin manipulation stage, it is necessary to apply microwave (MW) radiation in order to drive the transitions between spin sublevels. On condition that the applied MW frequency matches the $m_S = 0$ and $m_S = \pm 1$ energy gap, the population is shifted towards $m_S = \pm 1$ states, thus increasing the probability of the ISC path.

The increased probability of ISC, in turn, results in PL intensity reduction, serving as a readout signal. Therefore, external perturbations, such as magnetic, electric fields [72,73], temperature [74,75], pressure [76], or others that affect the spin levels can be detected as a corresponding drop in PL signal under matching microwave frequency application (Doherty et al. 2013) (Figure 3b).

Due to the NV⁻ color center's long spin coherence time at room conditions, with values reaching milliseconds, it allows detection of very weak signals through precise resonance shifts [40]. To the best of our knowledge, the highest sensitivity of diamond quantum magnetometry amounts to sub-10 pT ·Hz^{1/2} and was demonstrated in the work [77] with the sensor based on NV⁻ ensemble in a single-crystal diamond.

Despite the vital advantages in high sensitivity of spin-based quantum sensing approaches, in practice, the necessity of spin-manipulation provided by microwave application imposes practical limitations in design simplicity, sensor miniaturization, and integration, thus restricting the applicability in many real-world fields such as biological systems.

And disadvantages mentioned above motivate numerous research groups to explore alternative approaches, enabling them to avoid microwave applications. And another approach — sensing perturbations all-optically — offers a simplified decision while enabling sensors integration, miniaturization, and scalability as well as avoiding the side-effects of microwave delivery: local heating and electromagnetic interference.

2.3.2 All-optical quantum sensing

All-optical quantum sensing is based on changes in purely optical signatures such as color centers PL intensity, PL lifetime, spectral shifts (ZPL shift, FWHM broadening), or spin-lattice relaxation time (T_1) and could be implemented without a classical sensing stage, such as spin-state initialization and manipulation.

Further, several methods for implementing all-optical sensing with different color centers and for various physical parameters are considered.

1) Intensity-based all-optical magnetic field sensing with NV⁻ color center

In their work [78] authors consider the application of all-optical NV⁻ sensing to define high off-axis magnetic field values based on PL intensity changes. In the formula of ground-state spin Hamiltonian (1), the hyperfine interaction term H_{HF} could be omitted and present the Hamiltonian as a sum (3) of Longitudinal Zeeman interaction (4), and Transverse Zeeman interaction (5):

$$H_{gs} = hD_{gs}S_z^2 + g\mu_B \mathbf{B} \cdot \mathbf{S} = H_{gs}^z + H_{gs}^\perp$$
 (3)

$$H_{gs}^z = hD_{gs}S_z^2 + g\mu_B B_z S_z^2 \tag{4}$$

$$H_{gs}^{\perp} = g \mu_B (B_x S_x + B_y S_y) \tag{5}$$

It could be clearly seen from equation 2.5 that the Transverse Zeeman Interaction term occurs in the presence of transverse magnetic field components (B_x , B_y) imposing the mixing of spin sublevels $m_S = 0$ and $m_S = \pm 1$ on the energy level diagram of NV⁻ color center. The mix of spin sublevels means that the population of electron with initial spin state $m_S = 0$ is leaking to $m_S = \pm 1$ which, in turn, causes more non-radiative relaxation through the singlet states (dark state) and thus PL quenching. Authors demonstrated that this effect enables magnetic imaging using PL mapping based on a scanning NV⁻ microscope.

2) Lifetime-based magnetic field sensing with NV⁰ and NV⁻ PL

Horsthemke et al. [35] in their work proposed another suggestion of all-optical sensing based on PL lifetime – the average time a color center stays in its excited state before emitting a photon and returning to the ground state. The motivation behind this work is to propose the intensity-insensitive method since the intensity can be subjected to alterations caused by movement in the optical fiber or laser intensity fluctuations and thus affecting the sensing result. Authors demonstrated ~15.2% lifetime contrast in the presence of a magnetic field employing a MW-free fiber-based setup, thus demonstrating the feasibility of magnetic field sensing, which can be implemented in harsh conditions.

3) ZPL shift- and FWHM broadening-based all-optical thermometry with NV⁻ and SiV⁻ color centers

In the work [38] authors proved the feasibility all-optical thermometry with diamond microneedles containing NV $^-$ and SiV $^-$ centers. Authors demonstrated the ZPL redshift as well as FWHM broadening with temperature increase over the physiological range (25–55 °C).

To understand the physics behind these spectral signature changes, the energy level diagram of color centers (Figures 3b and 4) should be considered again. The ZPL emission corresponds to the direct electronic transition between ground and excited states of a color center, with no phonon involvement. If temperature increases, the diamond lattice undergoes thermal expansion, which results in increased phonon occupation. This stronger lattice vibrations cause the distortion of ground and excited energy levels, the energy gap becomes narrower, thus ZPL is shifting towards longer wavelengths [79]. This described enhanced electron-phonon interactions also

dynamically perturb the energy levels of color centers, resulting in inhomogeneous broadening, which could be observable as a zero-phonon line FWHM broadening [79].

4) NV⁻ relaxation time (T₁) sensing of magnetic field fluctuations

As was already stated in the introduction, the first direct mention of all-optical quantum sensing is attributed to the work [16]. Authors pioneered the method by using NV⁻ longitudinal spin relaxation time (T₁) detection, with which it was possible to sense fluctuations of the magnetic field. The developed method of detection was implemented for room temperature, relying on optical spin initialization and readout and avoiding microwave spin manipulation. To understand the physical principle behind this method, the term longitudinal spin relaxation time (T1) should be considered first. The longitudinal spin relaxation time (T_1) – time it takes for the spin system, such as NV⁻ color center spin, to return to its thermal equilibrium population along the magnetic field direction (z-axis) after being perturbed. Considering the energy level diagram of NV⁻ color center (Figure 2b), and situation where NV⁻ center's spin is polarized into a certain state $m_s = 0$ using a laser, it could be seen that T_1 here is duration of spin populations to "relax" back to their normal distribution with some repopulation of the $m_S = \pm 1$ states. Magnetic field fluctuations can drive transitions between spin states $m_S = 0$ and $m_S = \pm 1$, thus reducing the relaxation time. The stronger or more resonant these fluctuations are, the shorter the T₁ becomes, serving as a sensitive method and allowing room temperature magnetic sensing down to one molecule.

As can be seen from the provided review on diamond color centers in alloptical quantum sensing applications, the most widely used is still the NV⁻ center, although the SiV⁻ center is becoming increasingly common in articles devoted to quantum sensing. Other diamond color centers, despite attracting theoretical interest, are less frequently encountered in application-oriented studies. Some of them, however, exhibit ODMR and may attract growing attention for quantum sensing applications in the coming years, similar to what was seen for the SiV⁻ center. Notable examples include ST1 [80], TR12 [81], and ST2 center [82].

Beyond these, the present work turns to the 389 nm and 468 nm centers, which are also naturally formed in diamond needles [28,32]. Their spectral positions in the blue and green ranges could potentially extend the operational wavelengths of diamond-based platforms, as well as broaden the scope of all-optical sensing applications.

3 Materials and Methods

3.1 Description of SCDNs synthesis

For this study, SCDNs were synthesized using the PE-CVD method. The synthesis procedure has been comprehensively described in previous works [62,83] and will be briefly outlined in this thesis. A direct current PE-CVD system was employed with parameters such as substrate temperature (~900 °C), chamber pressure, and plasma power optimized for vertical needle growth. The growth was conducted using a gas mixture of hydrogen and methane on silicon or niobium substrates. The silicon substrates were used in the samples where the SiV centers formation was aimed while the niobium substrates allowed minimize the SiV centers concentration [33]. The typical process of SCDNs synthesis consists of two stages:

- 1. PE-CVD stage during which the films containing SCDNs surrounded by non-diamond phase or carbon matrix would be obtained;
- 2. Films oxidation on air (630 $^{\circ}$ C, 100 h) stage during which the material around SCDNs would be removed in the form of CO and CO₂ gases, revealing the final SCDNs form (Figure 5 b and c).

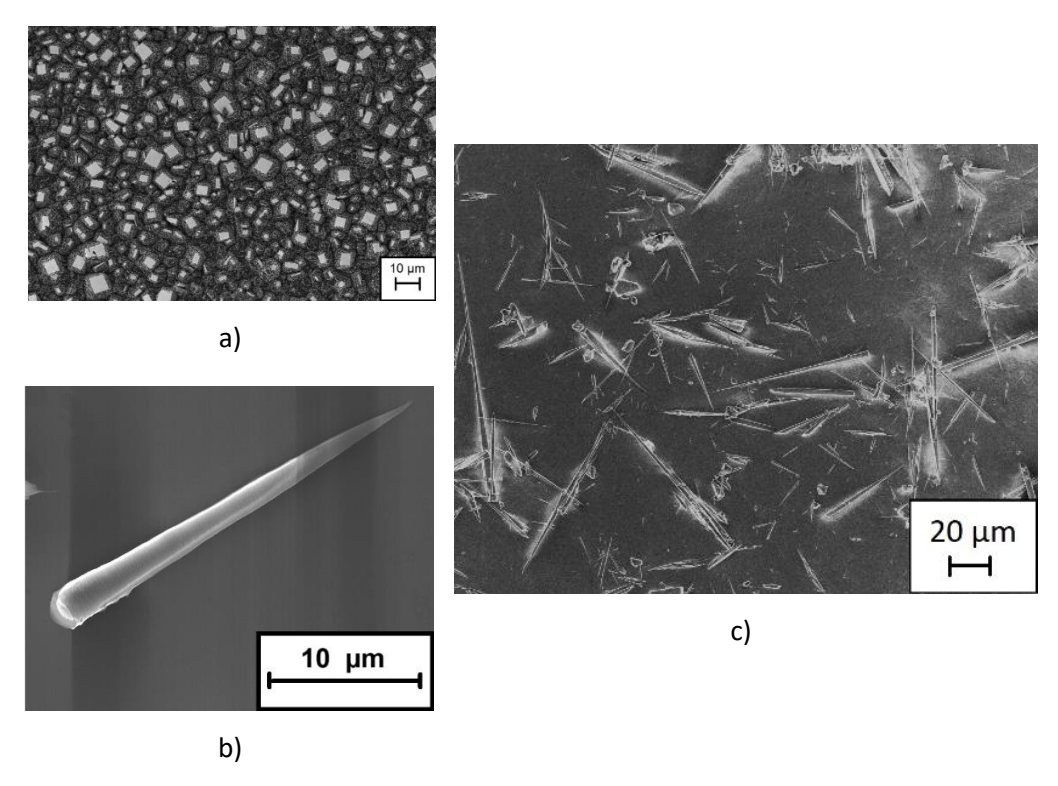


Figure 5. SEM images of a) — grown carbon films containing SCDNs, b) — individual SCDN, c) —. SCDNs after carbon film oxidation and precipitation on silicon plate for further analysis

To investigate how variations in gas composition during CVD growth influence the formation and optical behavior of color centers in SCDNs, seven samples with different methane concentrations, ranging from 0.8% to 5,3%, were synthesized. In addition, one sample was fabricated with 2,3% of methane and 0,05% of nitrogen to

gain insight into the influence of nitrogen incorporation on color center formation and charge-state behavior.

Once grown, the SCDNs-containing films undergo preparation for further analysis. For this purpose, pieces of the synthesized films were detached from the Nb plate, transferred onto polished silicon substrates, and subsequently oxidized. The resulting substrates with diamond needles were then used in the experiments.

3.2 Room-temperature experimental setup

To analyze the influence of gas composition during CVD growth on color center formation, the steady-state PL and time-resolved PL measurements were performed using an Edinburgh Instruments FLS1000 Spectrofluorometer (Figure 6). The performed measurements on spectrofluorometer are based on the luminescence principle, when a sample absorbs photons of specific energy and subsequently reemits photons at longer wavelengths. In the case of color centers in diamond, this process is conditioned by the electronic transitions between defect-related ground and excited levels within the diamond bandgap, and results in well-defined spectral features such as ZPLs and PSBs.

The spectrofluorometer is equipped with two monochromators on the excitation path and emission paths to isolate a specific wavelength from a broader spectrum. The excitation path starts with one of the available excitation sources: a steady-state xenon arc lamp, a picosecond pulsed diode laser with 377 nm central wavelength, and a picosecond pulsed diode laser with 504 nm central wavelength. To capture the emitting signal from the analyzed sample, the emission path ends with a single-photon detector (Figure 6). The spectrofluorometer is also equipped with a measurement chamber and a set of holders that ensure reliable and secure sample placement, designed to avoid obstruction of the excitation and emission paths.

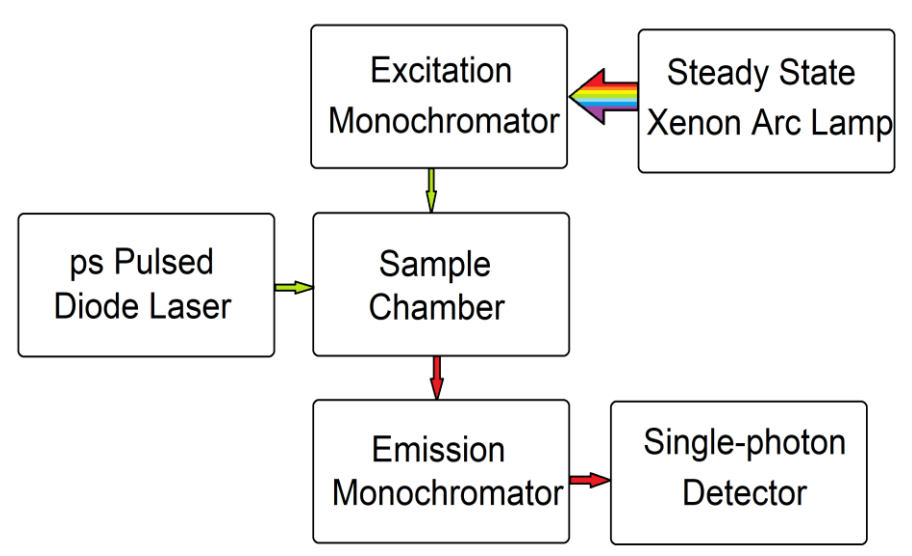


Figure 6. The schematic representation of FLS1000 Spectrofluorometer (adapted from https://www.edinst.com/products/fls1000-photoluminescence-spectrometer/).

Steady-state PL spectroscopy is a technique used to measure the emission of PL from a material under continuous excitation. In this technique, the emitted signal is collected and analyzed in terms of intensity vs. wavelength, thus obtaining an emission spectrum. The system is in a steady state since the rate of excitation and emission remains constant over time [84].

With the help of steady-state PL spectroscopy, the excitation-emission maps (EEMs) for each sample were acquired in the excitation range 250-700 nm with a step of 10 nm and emission recorded from 270 to 900 nm with a step of 1 nm. The width of the excitation slit was varied from 3 to 5 nm while the width of the emission slit was set to 1 nm. To avoid the passage of the excitation signal to the detector, all spectra were measured with an indentation of 20 nm from the excitation wavelength and before the doubled excitation wavelength.

Time-resolved PL spectroscopy is a technique used to determine the dynamics of excited states in materials by recording how the PL intensity decays over time after pulsed optical excitation [84].

With the help of time-resolved PL, the PL decay curves of different color centers were acquired to determine the corresponding PL lifetimes.

The measurements were performed using the time-correlated single photon counting (TCSPC) technique – a highly sensitive method that detects the arrival times of individual photons relative to the excitation pulse [84]. The system builds a histogram of photon arrival times for many excitation cycles, resulting in a time-resolved decay curve. This technique serves well for single-photon emitters or low-concentration color centers. To implement the TCSPC technique, pulsed excitation sources were employed: a picosecond-pulse laser with wavelengths of 377 nm or 504 nm was used to excite the corresponding color centers. The emission slit width was varied between 2 and 10 nm depending on the signal strength. The laser repetition rate was adjusted to provide pulse periods in the range of 200–500 ns, and data acquisition continued until the collected photons in the curve maximum reached approximately 10,000 counts. For lifetime extraction, the obtained decay curves were processed using Origin 2025 software. A custom-developed function was used to perform convolution with the instrument response function (IRF), followed by multiexponential fitting to retrieve the characteristic decay times.

The process of fitting PL decay curves and lifetime components decay evaluation is described in numerous works, including [32], and briefly provided below. Once the PL decay curves are obtained and the corresponding instrument response function (IRF) is measured, the incremental fitting with exponential decay models is performed. For each PL decay curve, the fitting starts with application of a monoexponential function (equation 3.1.), assuming a single decay component [85], and progresses to more complex multi-exponential models until the necessary match with experimental curves is achieved.

$$y_{fit} = y_0 + A_1 \exp\left(-\frac{t}{t_1}\right)$$
 (6)

where y_0 is the baseline, A_1 is the amplitude, and t_1 is the corresponding decay time.

The quality of fitting was evaluated using two statistical parameters: the reduced chi-squared (χ_R^2) and the coefficient of determination (R²). The reduced chi-squared is defined as $\chi_R^2 = \chi^2/(N-p)$, where N is the number of experimental points and p the number of fitting parameters, and it shows how close the fitted curve is to the experimental data, with values around 1 indicating a good fit within the experimental error. The coefficient of determination R² shows how much of the data variation is explained by the model, and values close to 1 correspond to a better fit. In practice, it was difficult to reach exactly $\chi_R^2 = 1$, due to parameter coupling in multi-exponential fits. For that reason, the fitting was iteratively refined until χ_R^2 reached its minimum, and the corresponding model was taken as the most suitable one.

3.3 Temperature-controlled experimental setup: cryogenic and physiologically relevant range (25–50 °C)

The above-described equipment for PL analysis enables both steady-state and time-resolved measurements under ambient conditions. However, one of the main goals of this study was to evaluate the feasibility of all-optical temperature sensing, which requires precise control over the temperature range. To address this, temperature-regulation facilities — a cryostat (Oxford Instruments Optistat DN) and a Thermal Controller (Oxford ICT 4) — were integrated into the spectrofluorometer setup (Figure 7). This integration allows to conduct PL measurements across a wide thermal range — from cryogenic conditions (using liquid nitrogen) up to physiologically relevant temperatures (25–50 °C).

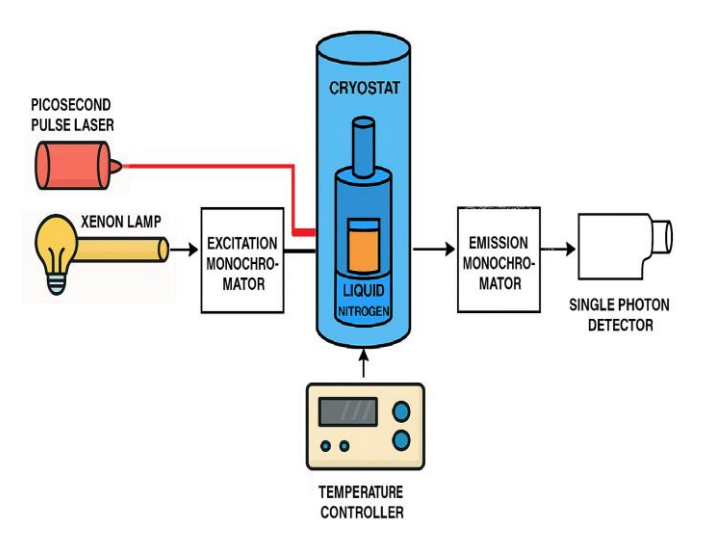


Figure 7. The schematic representation of temperature-controlled experimental setup.

Aside from expanding the temperature range of all-optical quantum sensing, cryogenic PL measurements are crucial in revealing color centers fine spectral and dynamic features that are typically obscured at room temperature due to phonon-induced broadening. These fine features are also vital for a fundamental understanding of the thermally induced modifications in the optical and spin

properties of color centers, which, in turn, influence their performance in quantum sensing applications.

3.4 NV⁻ and NV^o concentration evaluation

Aside from the optical behavior analysis of color centers in SCDNs, another key task of this study focuses on the charge state analysis of NV centers formed under varying gas compositions. As already stated in the introduction, the NV⁻ color center is a widely acknowledged and utilized defect in quantum sensing applications; therefore, achieving control over its efficient formation is a crucial step in the development of diamond-based quantum sensing platforms. Therefore, the aim was to evaluate the relative concentrations of NV⁻ and NV⁰ centers in SCDNs grown using different methane concentrations (ranging from 1.6% to 5.3%) and to identify the gas composition window that favors efficient NV⁻ formation.

Equally important is the technical challenge to develop a reliable protocol for quantifying the NV charge states in diamond structures. The negatively charged (NV⁻) and neutral (NV⁰) states of the nitrogen-vacancy defect can both be optically excited using green light. Although their ZPLs are spectrally separated, at 637 nm and 575 nm, respectively, their PSBs significantly overlap (Figure 8) since NV⁰ PSB extends up to 750-800 nm. This spectral overlap complicates the direct decomposition of their contributions within the PL signal, making the determination of each charge state's concentration a non-trivial analytical problem.

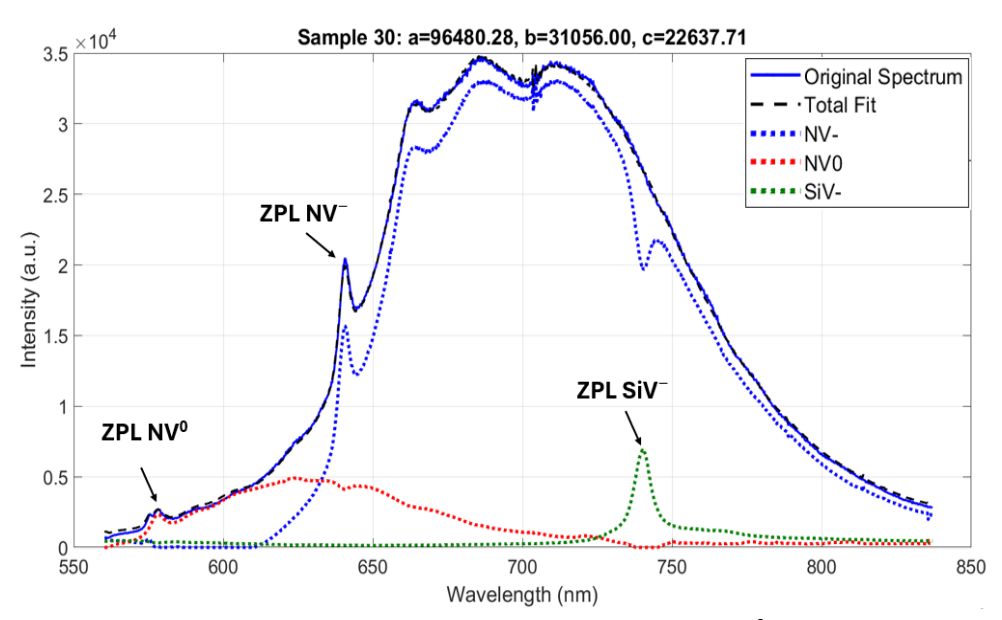


Figure 8. Typical PL spectrum at 532 nm excitation with NV⁻ and NV⁰ ZPLs at 637 nm and 575 nm, respectively, and overlapped PSBs. The ZPLs of NV⁻ and NV⁰ centers are marked with black arrows.

Therefore, in this section, the common approach used for determining the relative concentrations of color centers is outlined, followed by a detailed description of the developed spectral decomposition pipeline employed to quantify the contributions of NV⁻ and NV⁰ centers.

3.4.1. Concentration estimation via saturation curve fitting

One of the most widely accepted methods for quantifying emitter density is power-dependent saturation analysis [86]. In this method, the PL intensity is recorded as a function of excitation power. At low excitation power, the PL intensity grows approximately linearly, reflecting that the excitation rate is much lower than the decay rate. As the power increases, the excitation rate approaches the decay rate, and the emission tends toward an asymptotic maximum, which is described by the saturation model below:

$$I(P) = I_{sat} \frac{P}{P + P_{sat}} \tag{7}$$

where I_{sat} is the emission intensity at which the optical excitation rate from the ground state to the excited state equals the spontaneous decay rate back and P_{sat} is the excitation power at which $I=\frac{1}{2}I_{sat}$.

Since I_{sat} scales directly with the total number of identical emitters within the excitation volume, it is possible to determine the number of emitters in an ensemble:

$$N = \frac{I_{sat}}{I_{sat}^{(1)}} \tag{8}$$

where $I_{sat}^{(1)}$ is the saturation intensity of a single center that can also be determined by using the described approach. Dividing the number of emitters by the confocal excitation volume then yields the absolute concentration in cm-3 of active color centers.

In this work, the power vs. intensity curves were obtained by exciting SCDNs samples with a green continuous-wave (CW) laser using a confocal microscopy setup. The used confocal setup is described in detail in [33]. The spectra were recorded in the emission range 560-836 nm. The excitation power was varied in the range from 20 μW to 200 µW. For each combination of power and applied optical filter both PL spectrum and signal from single-photon counting module for each analyzed sample were measured. The detection pathway was equipped with two bandpass filters: 599/13 nm and 700/50 nm. In the case of the 599/13 nm filter, the recorded signal corresponds to the emission from the NV^o color center, while the NV⁻ contribution is effectively suppressed. This allows for the direct evaluation of NV⁰ concentration through the described power-dependent saturation analysis. On the other hand, the 700/50 nm filter transmits a large fraction of NV- PL around the PSB peak while including a contribution from the tail of the NV⁰ PSB. Therefore, in this case, the recorded signal is a composition of emissions from both charge states, making it necessary to perform spectral decomposition in order to accurately separate the NV⁻ component and evaluate the concentration. The applied decomposition procedure is described in the following section (3.4.2).

3.4.2 Spectral decomposition via non-negative matrix factorization

The task of spectra decomposition was solved with the Non-negative matrix factorization (NNMF) approach [87–89]. This approach allows for the decomposition of PL spectra into components that can be further interpreted by users while using the condition that all spectral intensities remain non-negative.

To perform the NNMF approach, the matrix factorization in the form below is used:

$$V \approx W \cdot H \tag{9}$$

where V is the $m \times n$ original data matrix. Each element represents a real, non-negative value corresponding to spectral intensity, the rows of the matrix are wavelength channels (m), and the columns are spectra (n). collected at different excitation powers, each normalized as a vector to unit length before decomposition.

Correspondingly, W is an $m \times r$ basis matrix containing the spectral profiles of the r components (such as NV $^-$, NV 0 etc.), and H is an $r \times n$ coefficient matrix that describes the relative contributions of each component in each spectrum.

in **MATLAB** The method can be realized with function [W, H] = nnmf(intensity, numComponents) and according to the function description in MATLAB: "The W and H matrices are chosen to minimize the objective function that is defined as the root mean squared residual between intensity and the approximation W·H. The factorization uses an iterative method starting with random initial values for W and H. Because the objective function often has local minimum, repeated factorizations may yield different W and H values. Sometimes the algorithm converges to solutions of lower rank than number of Components, and this is often an indication that the result is not optimal". In other words, NNMF works by minimizing the difference between the original matrix and the product $W \cdot H$, under the constraint that all entries remain ≥ 0 .

The decomposition procedure was applied to PL whole spectra acquired for each sample across various excitation powers. In this study, the decomposition involved three components: NV⁻, NV⁰, and SiV⁻, as some spectra were not pure combinations of NV⁻ and NV⁰ emissions but also included a contribution from the SiV⁻ component. According to the NNMF method description, it starts with random initial values for the W and H matrices. However, to improve the robustness and physical relevance of the decomposition, the process was guided by inputting reference spectra for NV⁻ and SiV⁻ as seeding shapes (Figure 9a). In this semi-supervised approach, only the NV⁰ component was extracted from scratch in the NNMF decomposition.

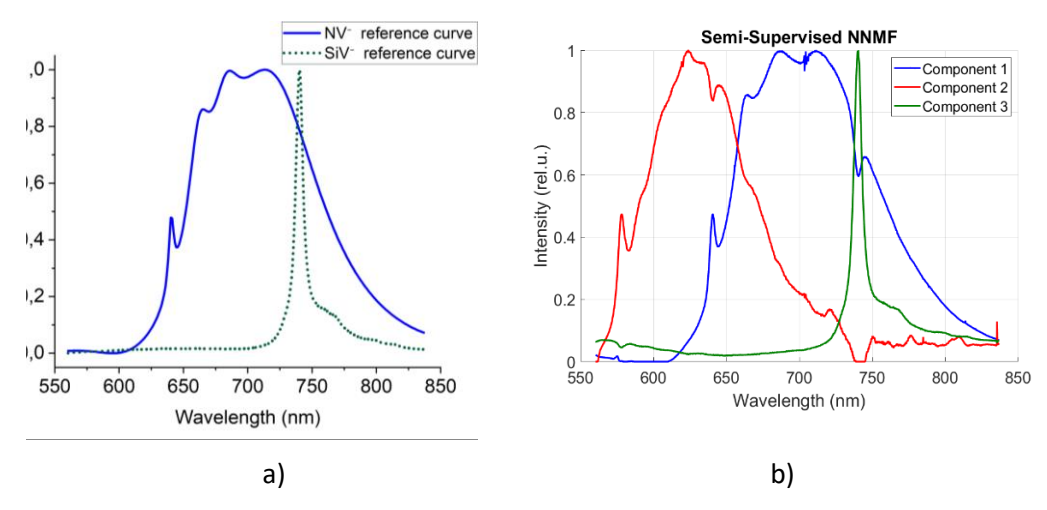


Figure 9. The NNMF decomposition procedure a) – inputs: NV⁻ and SiV⁻ reference curves as seeding shapes and b) – outputs: extracted shapes of three components.

It should be noted that due to NV⁰ contributions, the task of obtaining a reference spectrum for NV⁻ is not trivial. To isolate the NV⁻ spectrum, a special measurement setup with microwave excitation was utilized. When the microwaves are applied at the NV⁻ spin resonance, the NV⁻ emission undergoes a measurable change, while the NV⁰ contribution remains unaffected. By recording spectra with microwaves switched on and off and then calculating their difference, the part that changes can be attributed solely to NV⁻ (Figure 10).

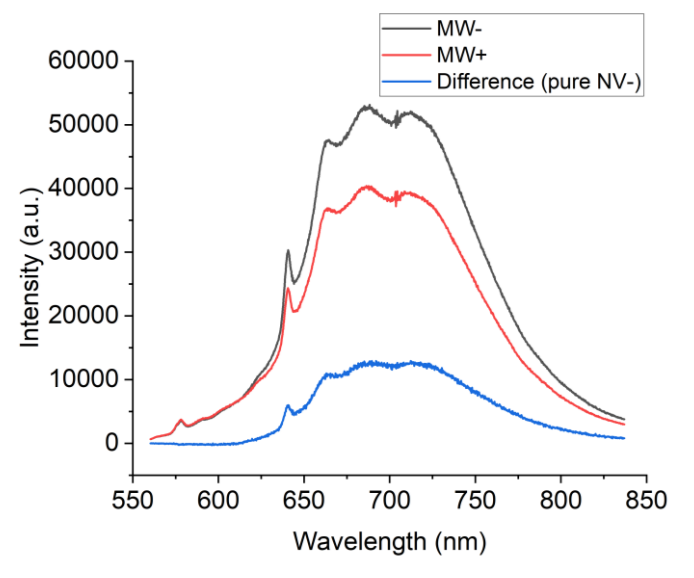


Figure 10. Typical PL spectra of the studied samples recorded in the 560–840 nm range without microwave excitation (MW–), with microwave excitation applied (MW+), and the corresponding difference spectrum, which reveals the pure NV⁻ contribution.

Analyzing the results of decomposition with the NNMF approach (Figure 10b), it should be noted that the method, even when guided by reference curves, does not yield perfectly separated component shapes. One artifact appears in the NV⁰

component around 638–641 nm, which can be attributed to the overlap with the strong ZPL of NV⁻ at 637 nm, introducing distortions in the decomposition. Another noticeable artifact is a dip in the NV⁻ component at 738–741 nm, originating from the overlap with the SiV⁻ ZPL at 738 nm. Despite these distortions, the main source of uncertainty arises from applying the overall NV⁰ component obtained from NNMF decomposition to each analyzed spectrum. To assess this systematic uncertainty, the NNMF-derived NV⁰ curve was compared with an etalon NV⁰ spectrum obtained from cathodoluminescence (CL) measurements (Figure 11). The areas under the corresponding spectra were calculated, and the discrepancy was found to be about 30%. This discrepancy was therefore assumed as the maximum uncertainty and further propagated into the calculations of NV⁰ and NV⁻ contributions.

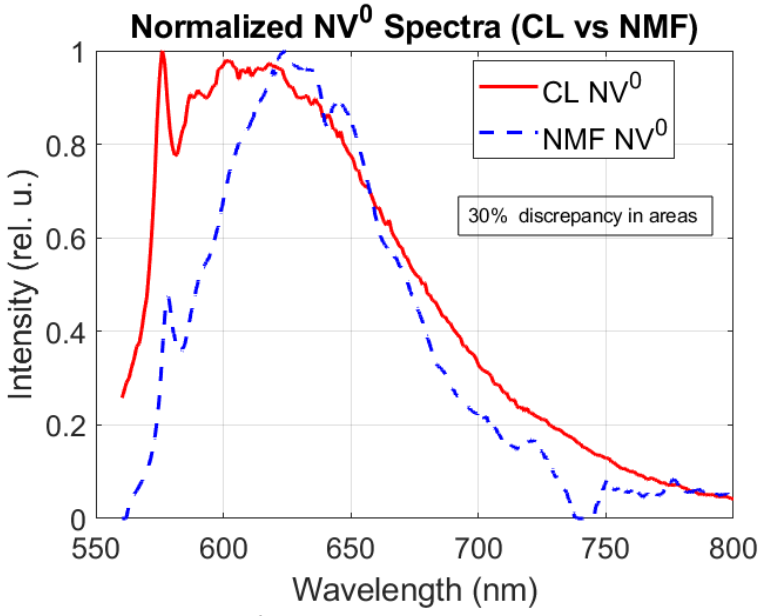


Figure 11. The comparison of decomposition-based NVO shape with etalon CL spectra to evaluate the systematic uncertainty.

Once the shapes of the components were extracted (Figure 9b), backfitting was applied to each spectrum to quantify the contribution of each component (Figure 12a). This procedure was followed by the application of a 700/50 nm bandpass filter (Figure 12b) to isolate the spectral region where NV⁻ and NV⁰ emissions overlap and the fraction of SiV⁻ PL signal is negligible. As the final step in the contribution analysis, the areas of the two components were calculated within the filtered region and expressed as percentages relative to the total area of the filtered spectrum (Figure 13).

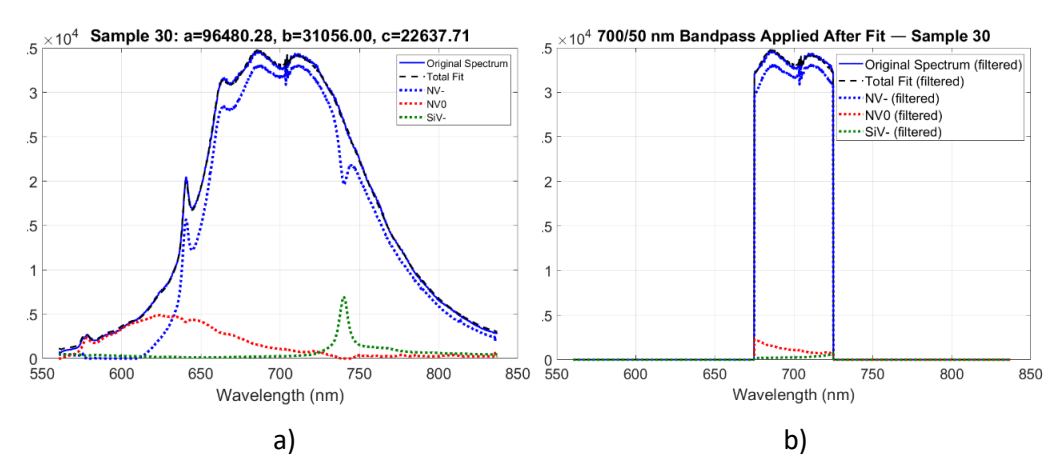


Figure 12. The decomposition spectrum with a) – back-fitting of the original spectrum (blue) using components for NV⁻, NV⁰, and SiV⁻ derived from NNMF. The numbers above the spectrum are the non-negative least squares scaling coefficients (a, b, c) obtained during the fit, which quantify the contribution strength of each component. b) – the same decomposition after applying a 700/50 nm bandpass filter.

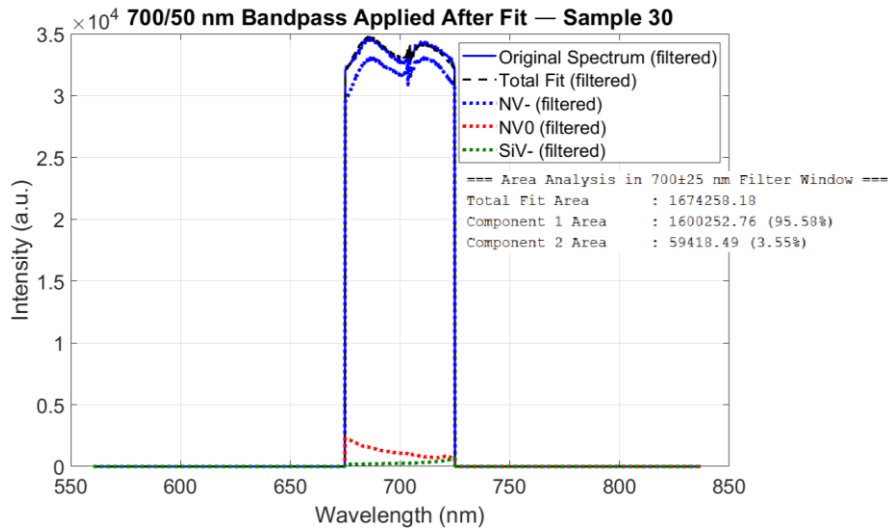


Figure 13. The decomposed spectrum using the 700/50 bandpass filter and the calculated contribution of each component.

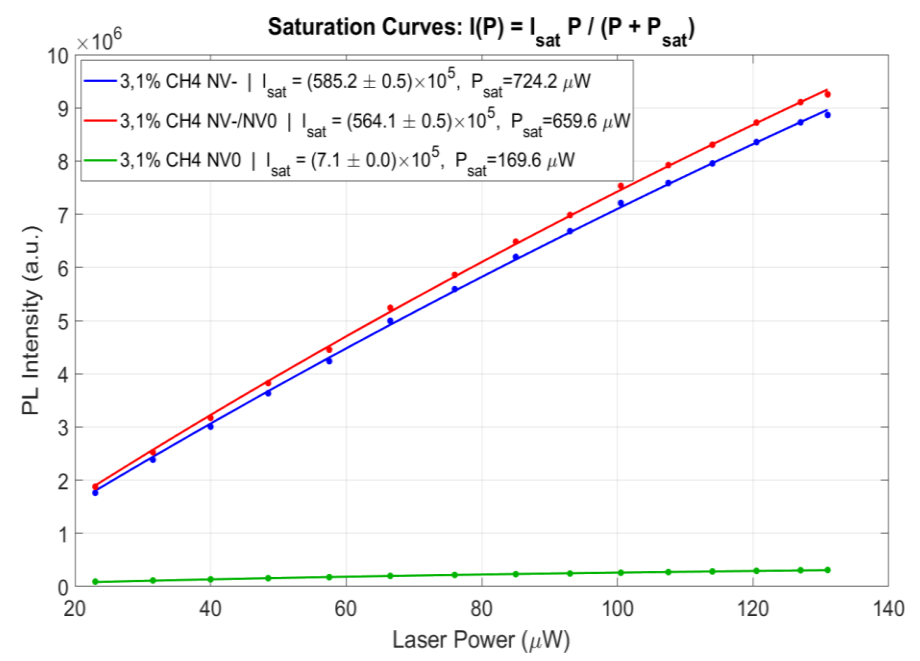


Figure 14. Power—intensity curves for the mixed NV⁻/NV⁰ emission and for the separated NV⁻ and NV⁰ components obtained from their calculated contributions. The saturation intensity values I_{sat}, extracted from fitting, are indicated in the graph legend.

These resulting percentages were then applied to the corresponding power vs. intensity curves (also obtained using the 700/50 nm bandpass filter) to generate the separated power vs. intensity curves for NV^- and NV^0 (Figure 14), according to their calculated contributions. All steps made allowed to apply the method described in section (3.4.1) to evaluate the corresponding concentrations of NV^- and NV^0 color centers in the samples.

4 Results and Discussion

4.1 General spectral characteristics of synthesized SCDNs

This section presents the steady-state PL analysis of SCDNs synthesized via the PE-CVD method, using various hydrogen-based gas compositions (Table 1). The corresponding emission spectra, recorded over different spectral ranges, are shown in Figure 15. Three excitation wavelengths – 350 nm, 420 nm, and 530 nm – were selected to demonstrate representative PL spectra, covering the entire spectral region relevant to diamond color center studies: from the 389 nm center in the near-UV range to the silicon-vacancy (SiV⁻) center with its ZPL at 738 nm. All presented spectra are normalized by maximum value in the collected spectral range.

Number of Sample	364	369	371	379	382	387	394	759
CH4,%	5,3	4,6	3,9	3,1	2,3	1,6	0,8	2,3
N ₂ ,%	-	-	-	-	-	-	-	0,05

Table 1. Gas composition parameters used for PE-CVD growth of SCDNs samples.

As can be seen from the PL spectra recorded at 350 nm excitation wavelength (Figure 15a, b), all samples show the presence of the 389 nm color center, with pronounced ZPL and clearly visible phonon replicas. Sample N364, grown with the highest methane concentration in the set, has a less pronounced 389 nm ZPL and only two visible phonon replicas. The partial obstruction of PSB for sample N364 is presumably related to the correction of spectra applied due to a pronounced setup-related artifact. The mentioned artifact manifests itself as a peak in emission spectra at around 410 nm, on condition that the overall emission signal is less than a certain intensity value. To minimize this artefact, the localized rescaling with a smooth taper to avoid this sudden jump was applied to this spectrum in MATLAB. The task of eliminating this artifact, although identified during the work, is beyond the scope of this thesis and will be addressed at the setup level in further research.

Only about half of the samples with methane concentration in the range 0,8–2,3% show the 468 nm color center with pronounced ZPL and replicas, and its intensity decreases as the methane concentration increases indicating decreasing ratio of 468 nm to 389 nm centers with the methane concentration growth. This excitation wavelength also reveals NV⁰ with a ZPL at 575 nm for all studied samples. It is also worth noting that the 533 nm color center is visible at 350 nm excitation in seven samples, except for the one grown with nitrogen addition (N759).

Analyzing the spectra obtained under 420 nm excitation, it can be observed that all samples exhibit the 468 nm color center, although its intensity is comparatively weaker in the N364 sample, demonstrating intense SiV⁻ PL. Since this excitation wavelength is also effective for SiV⁻ color center excitation [32], the latter is detected

in five of the investigated samples. The ratio of SiV⁻ to 468 nm centers is increasing with the growth of methane concentration.

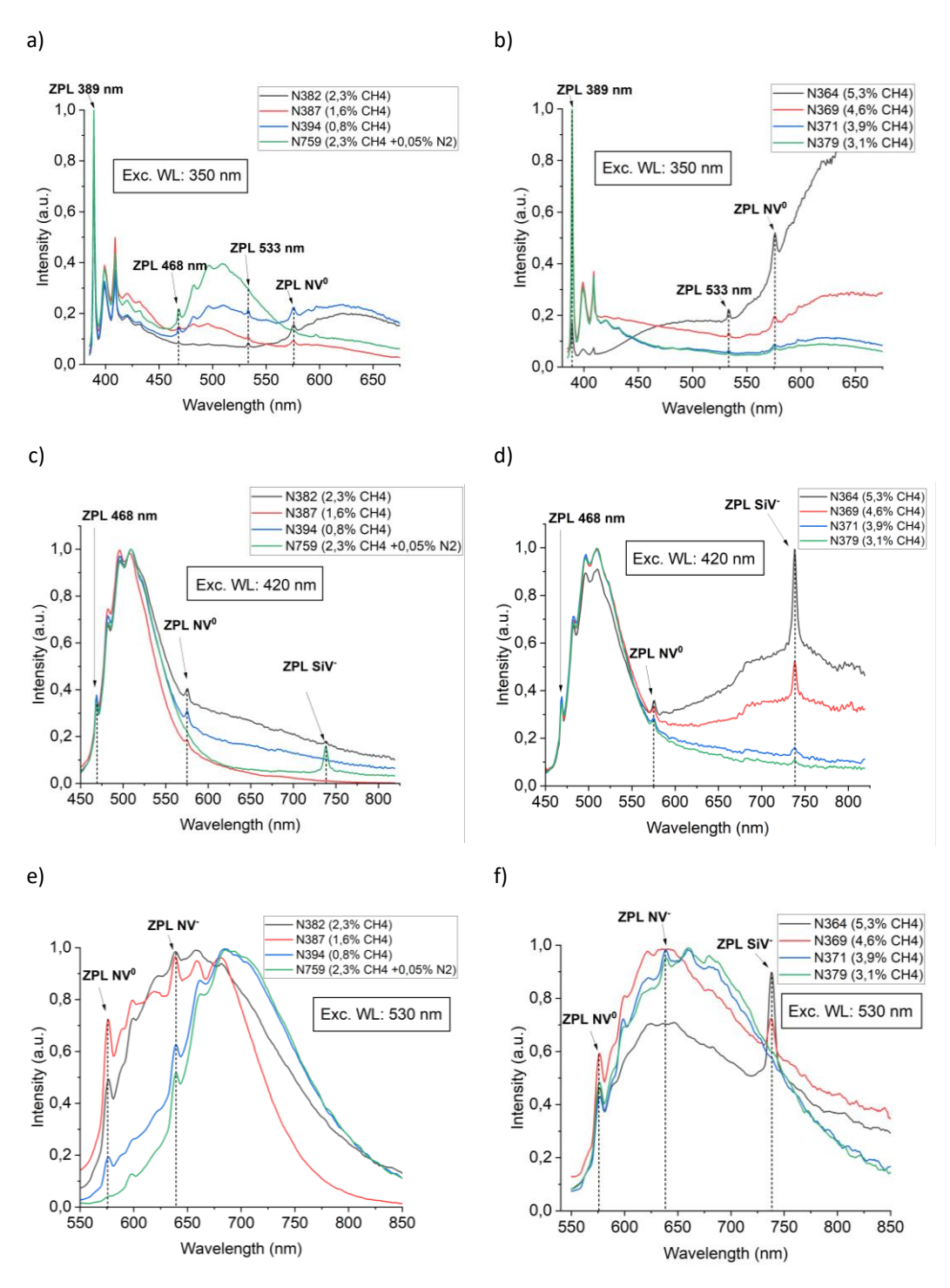


Figure 15. PL spectra of studied SCDNs obtained under different excitation wavelengths: a), b) -350 nm; c), d) -420 nm; e), f) -530 nm.

Finally, the 530 nm excitation allows a clearer detection of NV^0 color centers in all studied samples, and at the same time efficiently excites the NV^- color center with its ZPL at 637 nm. The latter is observed in all samples, but its presence is limited to those grown with methane concentrations in the range of 0,8-3,9%. Instead, for samples with high methane content (4,6-5,3%), the presence of SiV^- is documented. It is worth noting that samples N382 and N759 in Figure 15e demonstrate different ratio of NV^- to NV^0 lines despite the same methane concentration used in their synthesis. This could indicate that the addition of nitrogen into the gas mixture results in shift in balance of NV centers formation towards the preferential formation of NV^- centers.

Therefore, the PL spectra analysis revealed the presence of six distinct color centers, three of which are consistently observed in all studied samples. (389 nm, 468 nm, NV⁰).

After identifying the color centers, EEMs were recorded at room temperature for each studied sample to guide their selection for subsequent quantum sensing experiments. To facilitate the comparison, two complementary visualization approaches were applied to the EEMs data (Figures 16 and 17).

In Gallery A (global scale, Figure 16), all maps were plotted using a shared color scale set by the 2nd-98th percentile intensity range of the combined dataset. In theory, this approach makes it possible to compare absolute PL intensities between samples and to see which ones show stronger overall emission under the same excitation—emission conditions. Moreover, the comparison of absolute intensities between different samples can be considered as a rough tool for color center content comparison, provided that the active emitting volume within the excitation spot is similar for all samples.

Since all samples were prepared using the same protocol, this volume is expected to be similar. In practice, however, variations in the actual amount of material still influence the measured intensity. Therefore, in this work, the absolute intensity from EEMs is not used for quantitative conclusions on color center content, but rather as a practical guide for selecting samples that provide sufficiently strong signals from specific color centers for the next stages of experiments. Another disadvantage of such approach is that using a fixed scale means that low-intensity features in weaker samples can become less visible.

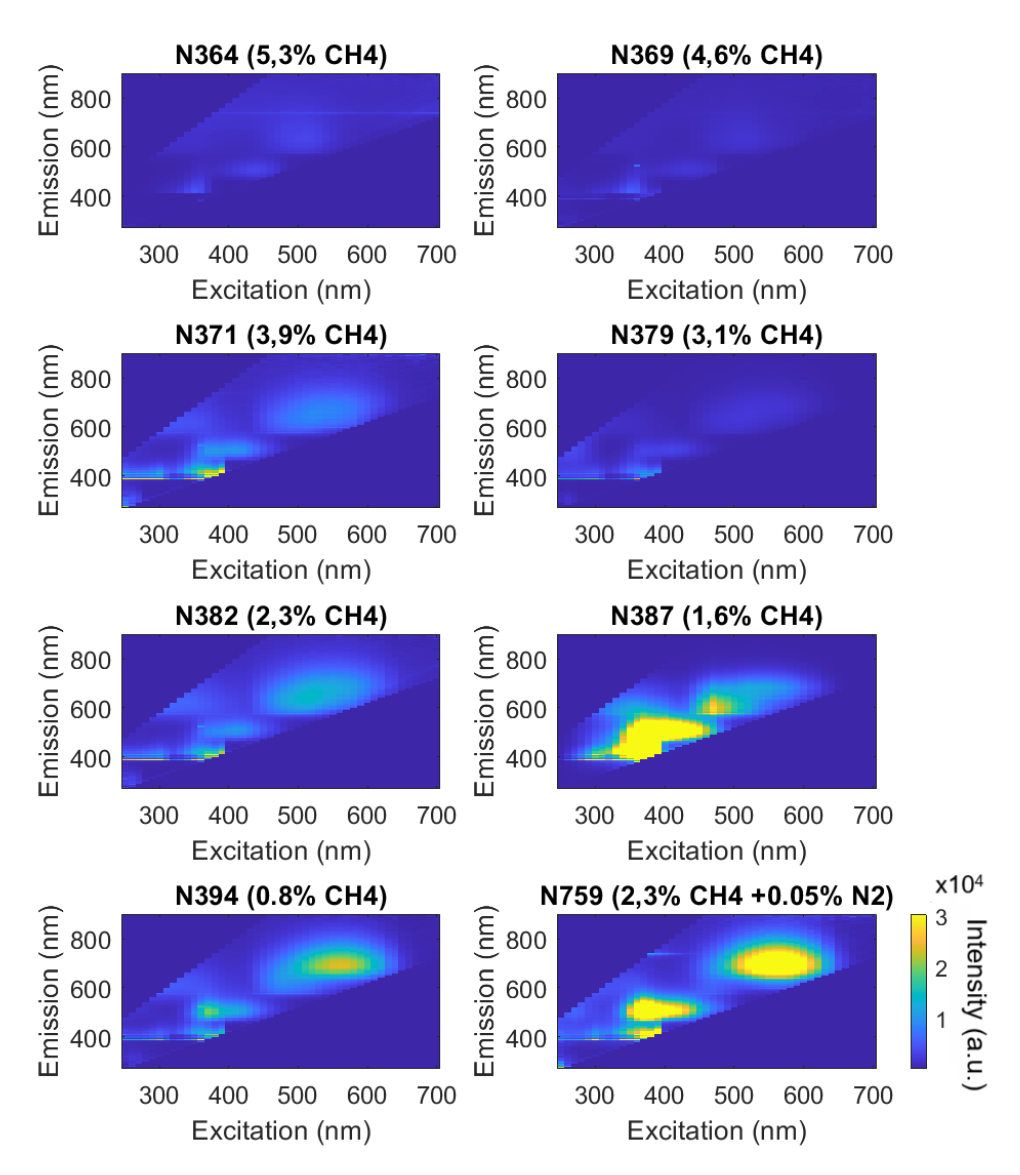


Figure 16. Gallery A with all maps plotted using a shared global color scale to facilitate the comparison of the absolute PL intensity between samples.

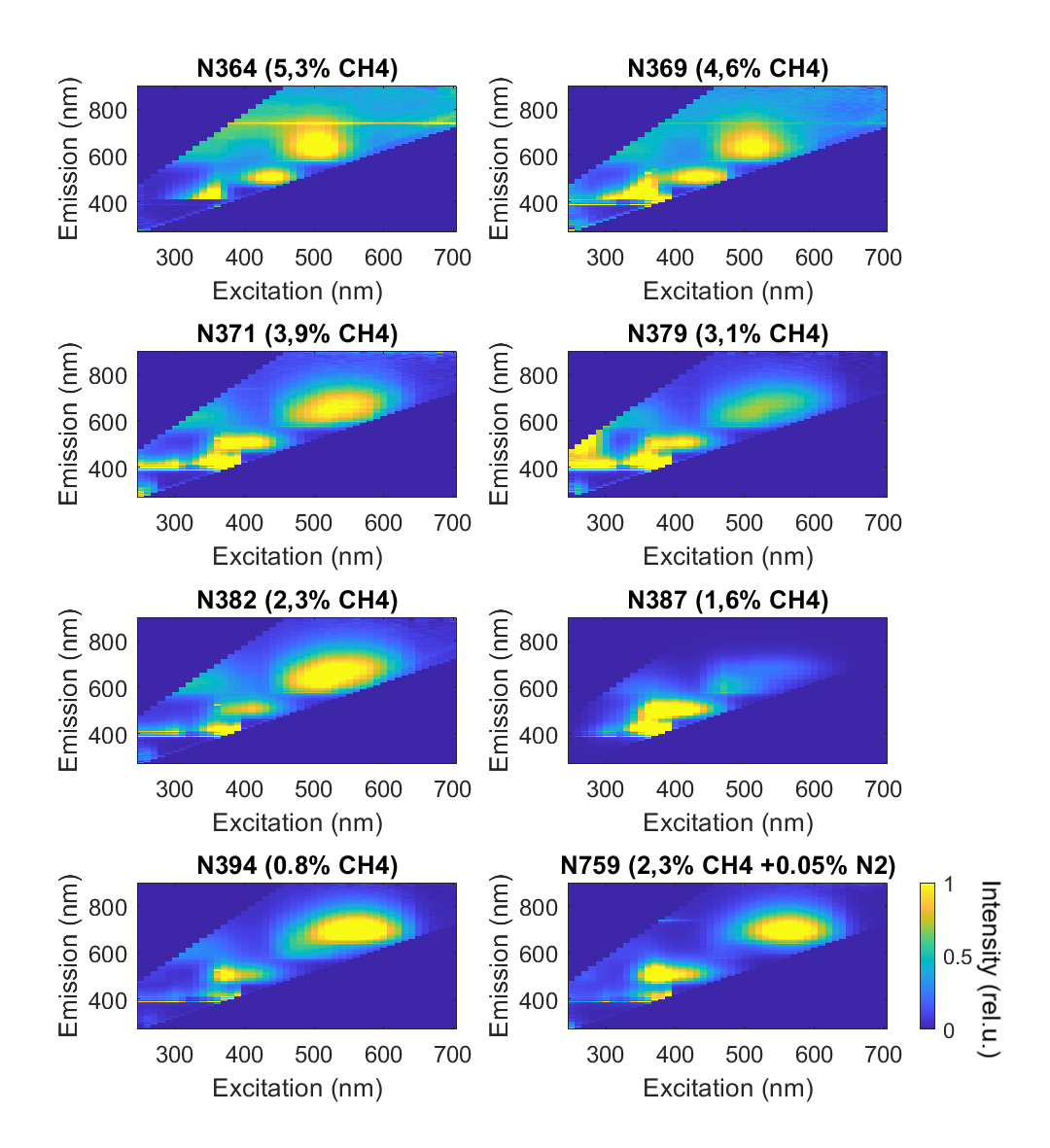


Figure 17. Gallery B with all maps individually normalized to its 95th percentile intensity to facilitate the assessing of the relative content of specific color centers across the samples.

In Gallery B (per-map normalized, Figure 17), each map was scaled to its 95th percentile intensity. This enhances the visibility of spectral features across the dataset, allowing even subtle peaks and PSBs to be seen in weaker emitters. Basically, this Gallery expands the results of emission spectra (Figure 15) by showing the signatures at other excitation wavelengths. While this method does not keep the absolute intensity differences between samples, it helps in evaluating the relative content of specific color centers.

Based on the Gallery A maps comparison, the strongest overall emission is observed for samples with 0,8% and 1,6% methane content, as well as for the sample with 2,3% methane content and 0,05% nitrogen addition.

From the comparison of Gallery B maps, the relative contributions of each color center within the samples were analyzed. The signatures corresponding to the

389 nm and 468 nm centers are intense across all samples, except for the 389 nm center in the sample grown with 5,3% methane. This suggests effective relative formation of these centers throughout the studied methane concentration range, with the notable reduction of the 389 nm center at the highest methane content (5,3%). Due to the strong spectral overlap of the NV^0 and NV^- , the EEMs analysis is less informative for these color centers. However, it can already be observed that the efficiency of NV center formation is less favorable at methane concentrations of 1,6% and 3,1% in comparison with the 389 nm and 468 nm centers. A more detailed analysis of NV^0 and NV^- formation will be presented in the following section.

Based on the comprehensive characterization of the samples' optical behavior, the sample grown with 1,6% methane and the sample grown with 2,3% methane and 0,05% nitrogen were selected for the next stage of the study. This is due to the strongest overall emission signal from the 389 nm and 468 nm color centers in these samples, while the further analysis was focused on evaluating the feasibility of alloptical sensing using these centers.

4.2 All-optical temperature sensing with 389 nm and 468 nm color centers

The first experiments on temperature-dependent all-optical sensing were conducted over a range from liquid nitrogen temperature (LNT \approx 81 K) to room temperature (RT \approx 295 K) in order to observe the overall response of the 389 nm and 468 nm color centers' optical signatures to temperature variations. Figure 18 shows the PL spectra recorded with a resolution step of 0,1 nm in the range of 385–460 nm at five different temperatures within the described range. In this experiment, the N387 sample was used due to strong PL emission from 389 nm color center. The excitation wavelength of 370 nm nm and slit of 5 nm for excitation and 0,1 nm for emission were used in these measurements. For each temperature, the ZPL position and its corresponding FWHM value were determined using a Gaussian fitting model (Figure 18), enabling the evaluation of spectral changes.

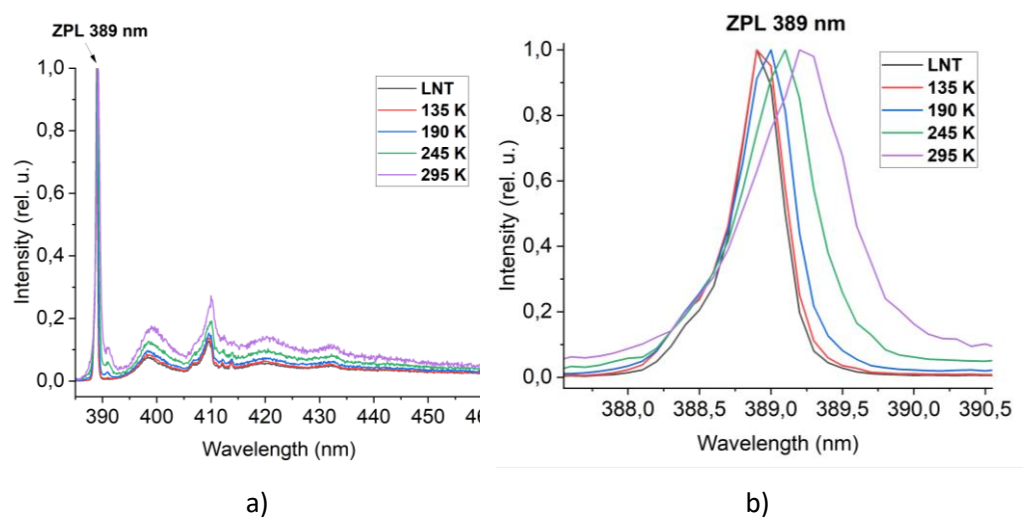


Figure 18. The emission spectra taken at different temperatures (LNT-RT), recording a) – full spectrum of 389 nm center including ZPL and corresponding PSB as well as b) – 389 nm ZPL only. All spectra are normalized by maximum.

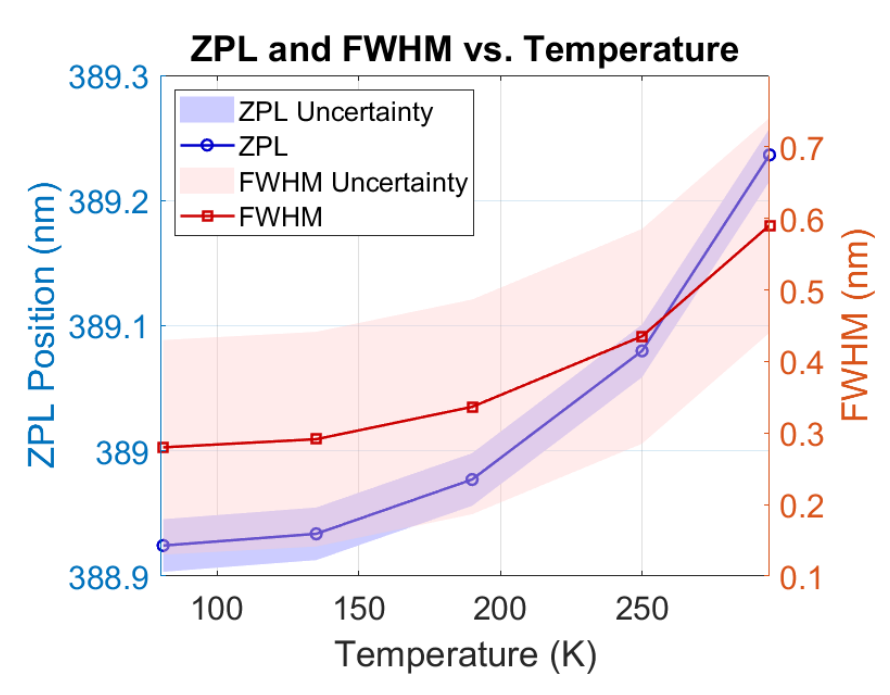


Figure 19. Temperature dependence of the 389 nm ZPL position and FWHM in the range from LNT to RT. Each uncertainty ribbon includes the corresponding standard deviation of repeated measurements together with the fitting error.

From the experimental data, it can be observed that the ZPL redshifts with increasing temperature: from 388,92 nm at LNT to 389.24 nm at RT. At the same time, the FWHM broadens from 0,28 nm to 0,59 nm. The calculated standard deviation of repeated measurements for the ZPL position is 0,02 nm, which is much smaller than the observed redshift (0,32 nm) and therefore does not significantly affect the interpretation of the temperature dependence. In contrast, the uncertainty in the FWHM measurements amounts to 0,15 nm, which is comparable to the observed broadening (0,31 nm) and thus limits its reliability as a sensing parameter.

In addition to ZPL position and FWHM, the ZPL intensity itself can also be monitored as a function of temperature. However, this approach has certain disadvantages: the measured values are strongly influenced by the optical setup, alignment, and detector response, and therefore require careful initial calibration. Given the complexity of the present setup, which involved a cryostat and temperature controller, such calibration was impractical, and the ZPL-intensity method was not implemented in this work.

For further comparison of the sensitivity of different methods, the results of the ZPL-temperature dependence were expressed as an average sensitivity value: the 389 nm center exhibits a total ZPL redshift of \approx 0,32 nm over the 81–295 K range, which corresponds to an average slope of \approx 0.0015 nm/K (1,5 pm/K).

Similar experiment was conducted for the 468 nm color center. In this experiment, the N759 sample was used due to strong PL emission from 468 nm color center. Figure 20 shows the PL spectra recorded with a resolution step of 0,1 nm in the range of 455–570 nm at five different temperatures within the described range.

For this color center, the ZPL redshifts with temperature, and FWHM broadening is also observed: from 467,77 nm at LNT to 468,36 nm at RT, and from 0,92 nm to 2,01 nm, respectively (Figure 20 and 21). The uncertainty ribbon does not obstruct the ZPL shift, confirming its reliability, while for the FWHM the uncertainty is comparable with the broadening, which limits its applicability as a sensing parameter. The average slope of ZPL vs. temperature curve $\approx 0,0028$ nm/K (2,8 pm/K).

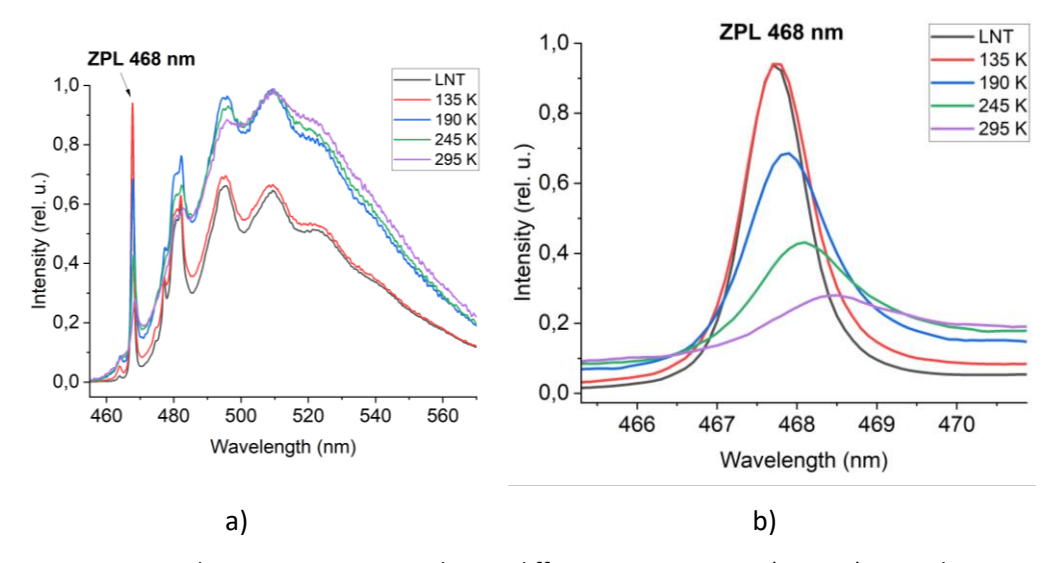


Figure 20. The emission spectra taken at different temperatures (LNT-RT), recording a) – 468 nm ZPL and corresponding PSB as well as b) – 468 nm ZPL. All spectra are normalized by maximum.

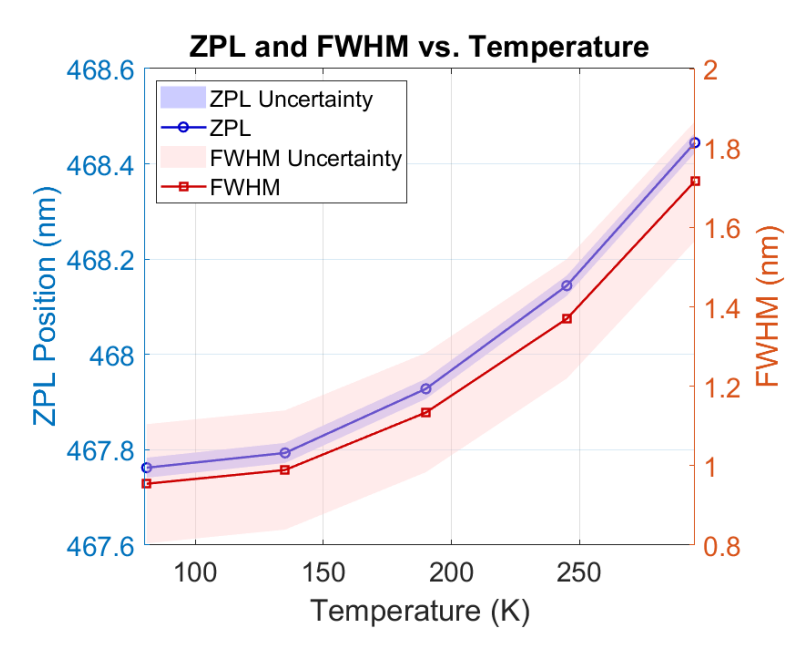


Figure 21. The dependences of 468 nm ZPL position and FWHM value on temperature in the range of LNT-RT.

Another parameter to consider for 468 nm based all-optical thermometry is the ratio of the ZPL intensity to third phonon replica (PR) intensity: while starting with value 1,5 at LNT it drops almost five times to RT (Figure 22b).

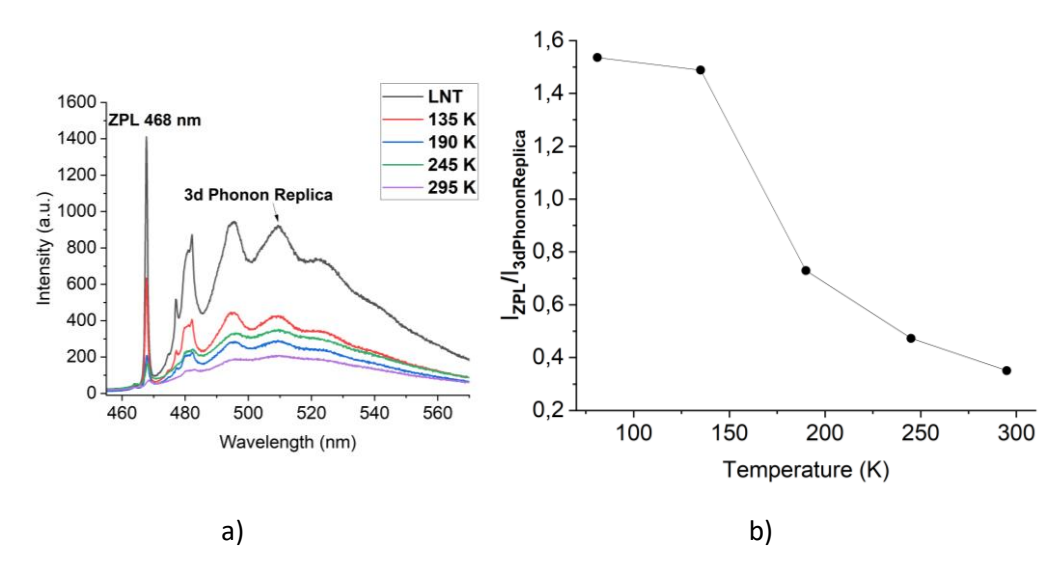


Figure 22. The emission spectra taken at different temperatures (LNT-RT), recording a) – 468 nm ZPL and corresponding PSB, not-normalized, displaying peaks' intensities change and b) – dependence of ZPL intensity to the 3rd PR intensity ratio on temperature.

To compare the ZPL-shift method with the ZPL/3rd PR ratio method, the **temperature resolutions** were calculated using expression (10) [90]:

$$\Delta T = \frac{\sigma_M}{\left|\frac{dM}{dT}\right|} \tag{10}$$

where M – measured quantity, σ_M – its uncertainty, and |dM/dT| – sensitivity (slope) in the temperature range of interest.

Table 2. summarizes calculated temperature resolutions for 389 nm and 468 nm ZPL shift and 468 nm ZPL/PSB ratio methods.

Color center	Method	Temperature resolutions, K
389 nm	ZPL shift	13,3
468 nm	ZPL shift	7,1
468 nm	ZPL/3 rd PR	8,2

Table 2. Temperature resolutions calculated for different all-optical thermometry methods.

Table 2 indicates that the ZPL shift of the 468 nm color center yields the highest temperature resolution among the evaluated methods.

The calculated temperature resolutions (Table 2), if compared with the subkelvin values already demonstrated in recent works and mentioned in the Theoretical background section, may not appear very competitive. However, these results most

probably reflect the limitations of the present setup, where the main constraining factors were the spectrometer resolution, calibration accuracy, and the overall signalto-noise ratio of the detected spectra. Another limiting factor was the estimation of measurement accuracy, which was derived as a standard deviation from only three repeated measurements taken, although at the same temperature points, however, during different cycles: heating and cooling. As a result, the conditions were not fully reproducible, leading to an overestimation of the uncertainty, particularly noticeable for the FWHM broadening. In principle, significantly better values could be achieved with optimized setup instrumentation. For the ZPL shift method, the resolution is determined by how precisely the ZPL position can be extracted, according to equation (10). In the present case, the fitting uncertainty of the ZPL position was about 0,02 nm, and with a measured slope of ~0,0015 nm/K this gives a resolution of several kelvin (Table 2). Modern high-resolution spectrometers, however, provide sub-picometer accuracy, and, with higher photon counts, the fitting uncertainty can be reduced by at least an order of magnitude. Under such conditions, the estimated resolution could reach the 0,1 K range or below. The ZPL/PR ratio method is more sensitive to alignment and calibration, but its performance could also be substantially improved, for example by employing dual-channel detection schemes.

Nonetheless, the concept of all-optical temperature sensing was demonstrated for the 389 nm and 468 nm color centers through their ZPL redshift, as well as through the change in the ZPL-to-3rd PR intensity ratio for the 468 nm center. At the same time, although FWHM broadening follows an observable trend, its applicability is limited by the relatively large standard deviation of repeated measurements. A more detailed investigation of this effect, including whether it is related to the experimental setup, requires further research that lies beyond the scope of this work.

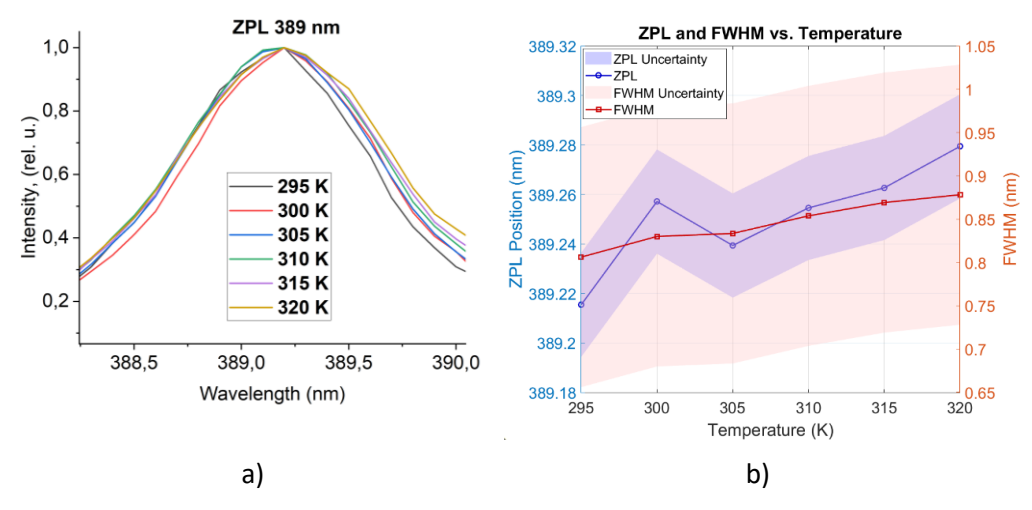


Figure 23. The recorded for 389 nm color center a) - ZPL at different temperatures (295 - 320 K) as well as b) - the dependences of 389 nm ZPL position and FWHM value on temperature in the range of 295 - 320 K.

Based on the above-mentioned proof-of-concept experiments, the research's next focus was on a narrower but practically important interval: biologically relevant temperatures, from RT (295 K) to $^{\sim}50$ °C (320 K). Unlike the LNT–RT study, this range requires closer temperature spacing between measurement points, since the overall interval is smaller and the expected spectral variations are subtler.

Figure 23 shows the 389 nm ZPLs recorded with a resolution step of 0,1 nm at five different temperatures within the biologically relevant interval, as well as the corresponding changes in ZPL position and FWHM within this range, presented together with the applied uncertainty framework.

Similar measurements were conducted for 468 nm ZPL nm (Figure 24).

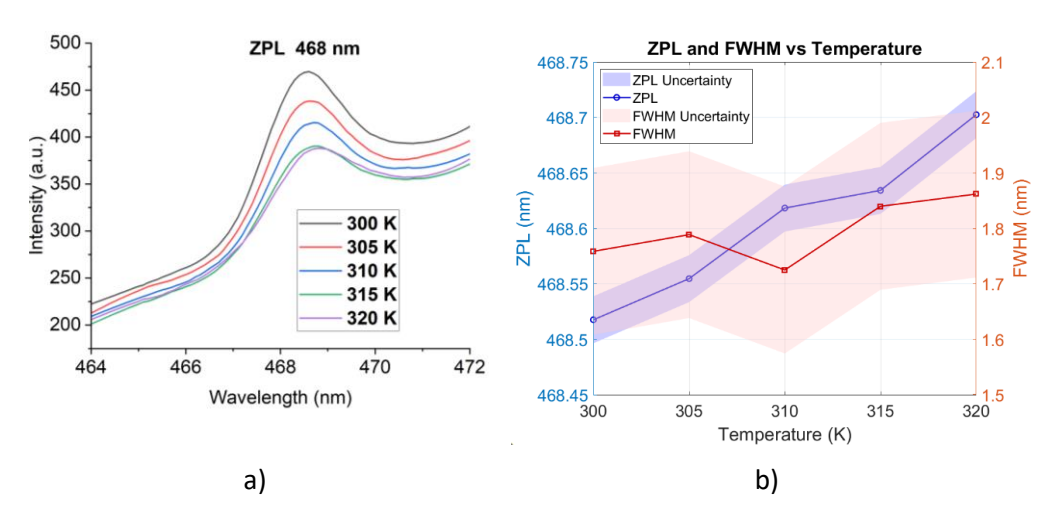


Figure 24. The recorded for 468 nm color center a) - ZPL at different temperatures (300 - 320 K) as well as b) - the dependences of 468 nm ZPL position and FWHM value on temperature in the range of 300 - 320 K.

For both color centers, it is seen that the uncertainty ribbon does not obstruct their ZPL shift, while for the FWHM, the uncertainty is comparable with the broadening. The calculated temperature resolutions for 389 nm and 468 nm ZPL shift amounts to 8,3 K and 2,2 K, respectively. Therefore, in the biological range of temperature, the 468 nm color center shows a much stronger ZPL shift than the 389 nm center.

Aside from spectral signature analysis, another approach – PL lifetime – was the next to be considered within all-optical thermometry research in the present work. The PL decay curves were taken at 399 nm emission to analyze the dynamics of the 389 nm color center. This wavelength was chosen to optimize signal collection using broad and bright enough phonon line of the center. Since the longest lifetime component of the 389 nm color center is of significant value, reaching 30 ns [32], the excitation repetition rate was set to give an interpulse period of 500 ns.

Figure 25 shows PL decay curves taken at different temperatures within the range from LNT (~81 K) to 290 K for the 389 nm center on a semi-logarithmic scale.

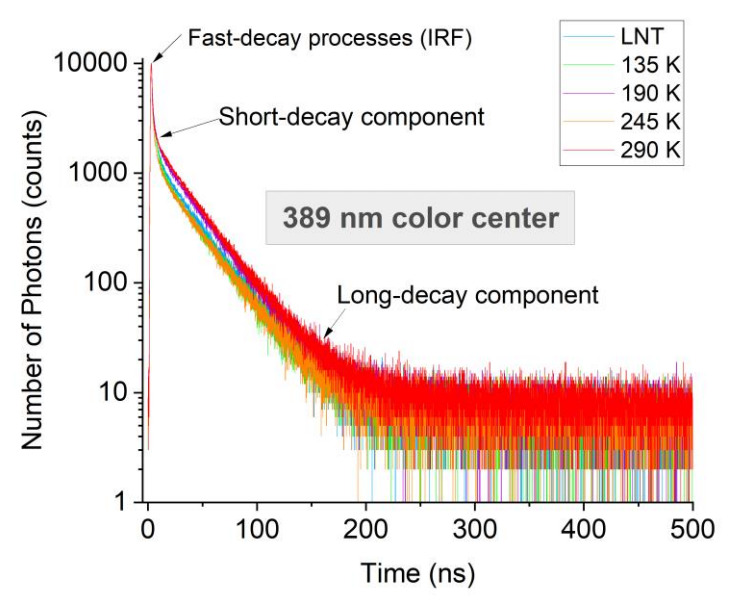


Figure 25. PL decay curves for the 389 nm color center on a semi-logarithmic scale.

The measured decay curves were analyzed by modeling the signal as a sum of three exponential components, convolved with the instrument response function (IRF). The convolution was conducted numerically (FFT-based), and the resulting model was fitted to the experimental data in order to extract the characteristic decay times and amplitudes. The retrieved parameters are summarized in Table 3. The fitting error does not exceed 2%.

Т, К	A ₁	t ₁ , ns	A ₂	t ₂ , ns	A ₃	t ₃ , ns
LNT	0,69	0,53	0,24	2,49	0,07	29,21
135	0,65	0,31	0,29	2,06	0,06	27,50
190	0,69	0,41	0,22	2,21	0,08	29,90
245	0,79	0,44	0,16	2,30	0,05	29,22
290	0,81	0,44	0,11	2,41	0,08	30,36

Table 3. The results of 389 nm color center PL decay curves fitting.

The PL decay analysis of the 389 nm color center revealed three lifetime components: a fast ($t_1 \approx 0.3-0.5$ ns), a short ($t_2 \approx 2.0-2.5$ ns), and a long ($t_3 \approx 27-30$ ns). None of these components exhibits a systematic trend with temperature, and their corresponding amplitudes follow a similar behavior. The only possible trend can be noted for the short-decay component demonstrating lifetime increase from 2,06 to

2,41 ns with simultaneous amplitude decrease from 0,29 to 0,11 with temperature growth in the range from 135 to 290 K.

The PL decay curves were taken at 481 nm emission to analyze the dynamics of the 468 nm color center, as well as avoiding the possible contribution of the 389 nm PSB tail. Since the longest PL lifetime component of the 468 nm center in SCNDs was determined to be 2,5 ns [32], the laser repetition rate was adjusted to provide an interpulse period of 200 ns. Figure 26 depicts the series of PL decays for the 468 nm color center on a semi-logarithmic scale.

The retrieved parameters of bi- or tri-exponential fitting are summarized in Table 4.

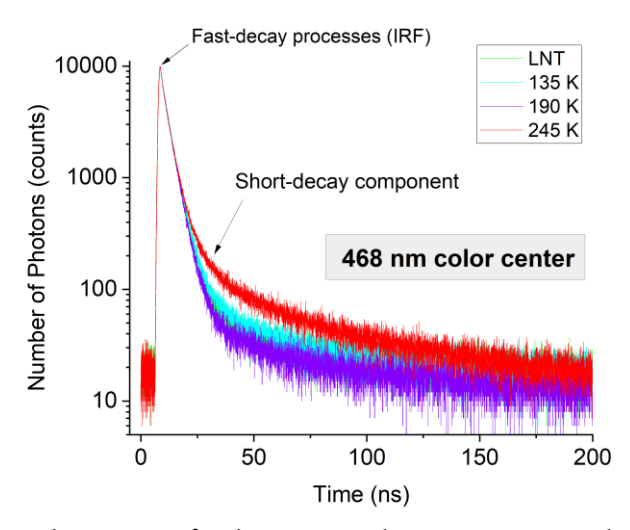


Figure 26. PL decay curves for the 468 nm color center on a semi-logarithmic scale.

Т, К	A ₁	t ₁ , ns	A ₂	t ₂ , ns	A ₃	t₃, ns
LNT	0,25	1,27	0,75	3,83	-	-
135	0,21	1,34	0,79	3,81	-	-
190	0,25	1,30	0,75	3,81	-	-
245	0,31	0,83	0,67	3,52	0,03	25,84

Table 4. The results of 468 nm color center PL decay curves fitting.

The PL decay analysis of the 468 nm center revealed two lifetime components: a fast component ($t_1 \approx 1,2-1,3$ ns) and a short component ($t_2 \approx 3,5-3,8$ ns) with stable relative amplitudes across the 80–190 K range. At 245 K, an additional long component ($t_3 \approx 26$ ns) emerged with a very small amplitude, which is most likely related to the increased influence of the 389 nm center PL tail rather than being an intrinsic feature of the 468 nm emission. The measured lifetime of 26 ns is a bit shorter than the value presented in the Table 3 for the 389 nm center at 295 K. However, the difference is probably related to limited accuracy of fitting method for components with such minor amplitudes. It can be concluded that the 468 nm color center is insensitive to

temperature in terms of PL lifetime, and therefore, lifetime-based thermometry is not suitable for this color center.

To sum up the section on all-optical thermometry with the 389 nm and 468 nm color centers, it was demonstrated that the sensing is feasible when considering spectral signatures, in particular the ZPL shift. In addition, the 468 nm center provides an alternative sensing approach through the analysis of the ZPL-to-3rd PR intensities ratio. A comparison of the extracted temperature resolution values indicates that the 468 nm center offers a slightly higher resolution than the 389 nm center. At the same time, both color centers do not demonstrate the systematic trend in lifetime changes. However, a more comprehensive investigation is required to conclude whether both color centers are truly insensitive to temperature in terms of PL lifetime, since for the 389 nm center one of the lifetime components shows a certain temperature dependence in the range of 135–290 K.

4.3 All-optical magnetic field sensing with 389 nm and 468 nm color centers

Having established the feasibility of temperature sensing, the focus can be shifted toward another sensing modality – the response of 389 nm and 468 nm color centers to magnetic field.

As in the case of the previously described all-optical thermometry with the 389 nm and 468 nm color centers, the feasibility of magnetic field all-optical sensing was analyzed by conducting two sets of experiments based on different optical signatures: emission spectra and PL decay times. These experiments were designed as proof-of-concept studies and therefore did not require controlled variation of the magnetic field strength. Instead, the signatures were recorded in two conditions: in the absence of a magnetic field and in the presence of a field generated by a neodymium magnet.

The PL spectra experiments started with creating conditions in which the well-known effect of PL quenching for NV⁻ color centers [78] could be observed. This effect, caused by spin state mixing under an off-axis magnetic field, was observed in our setup with SCDNs samples and demonstrated ~20% PL quenching (Figure 27) in the presence of a neodymium magnet. The magnet's position relative to the sample was then fixed as a reference and used in subsequent experiments with 389 nm and 468 nm color centers.

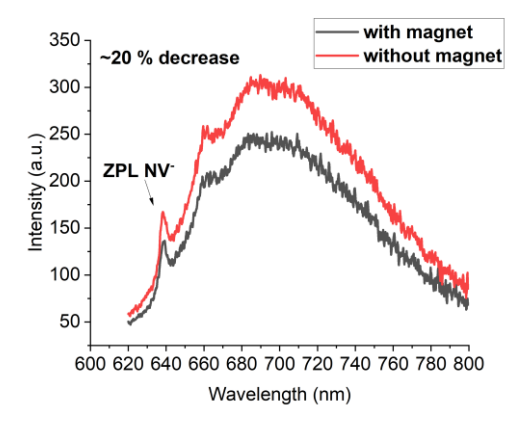


Figure 27. NV⁻ PL emission spectra recorded in the absence and presence of a magnetic field.

The experiment was then repeated for the PL emission spectra of the 389 nm and 468 nm color centers, which exhibited intensity decreases of about 10% and 10–15%, respectively, in the presence of a magnetic field (Figures 28 and 29).

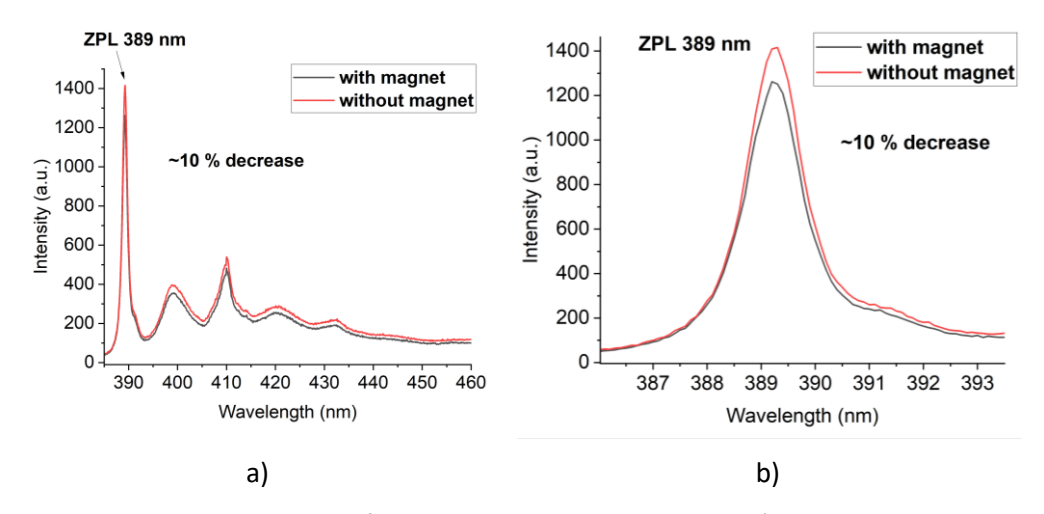


Figure 28. PL emission spectra of the 389 nm color center recorded a) – in the range 385–460 nm and b) – in the range 386–394 nm, in the absence and presence of a magnetic field.

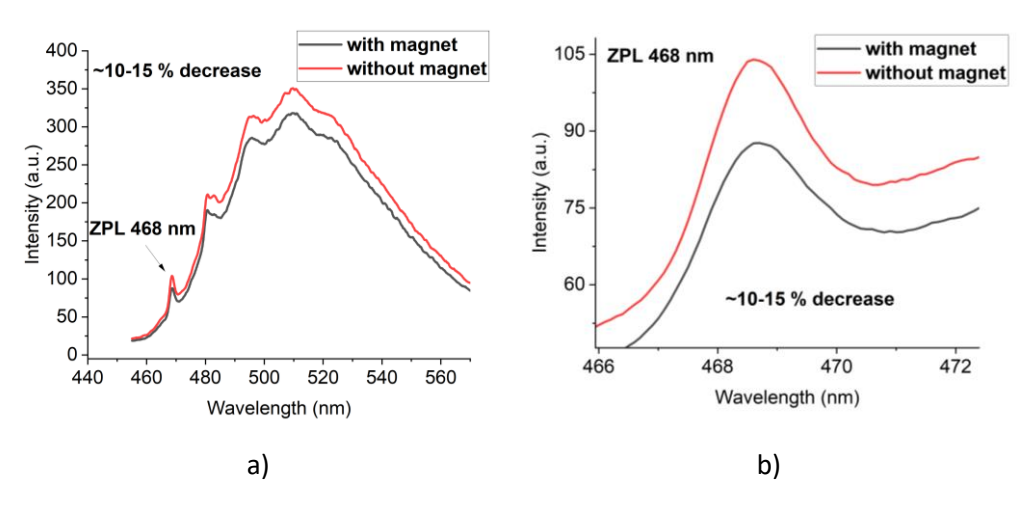


Figure 29. 468 nm PL emission spectra recorded a) – in the range 455-570 nm and b) – in the range 466-473 nm, in the absence and presence of a magnetic field.

Therefore, the proof-of-concept experiments revealed the feasibility of all-optical magnetometry based on the PL intensity quenching observed in the 389 nm and 468 nm color centers. However, additional analysis with controlled variation of the magnetic field strength is required to quantify the response and evaluate sensing performance.

The second set of experiments, focused on PL lifetime, was also started with the NV⁻ center in order to observe the previously reported reduction of lifetime under magnetic field conditions [35]. After confirming this reference behavior, the same proof-of-concept conditions were applied to the 389 nm and 468 nm color centers.

The PL decay curves were taken at 700 nm emission to analyze the dynamics of the NV⁻ color center, as well as minimizing effect of possible contribution of the NV⁰ PSB tail. Since the longest PL lifetime component of NV⁻ color center in SCNDs was determined to be 12 ns [32], the laser repetition rate was adjusted to provide an interpulse period of 200 ns. Figure 30 depicts two of the PL decays for the NV⁻ color center on a semi-logarithmic scale in the presence and absence of a magnetic field.

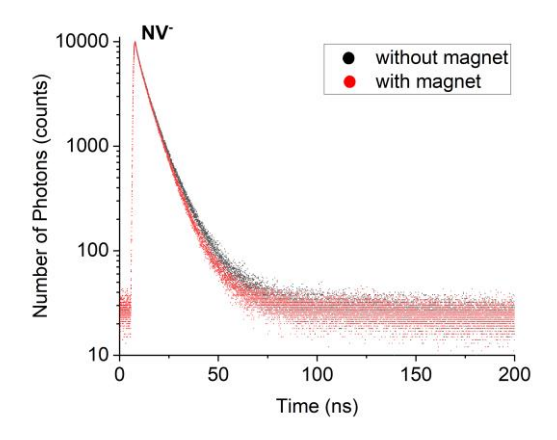


Figure 30. PL decay curves for the NV⁻ color center on a semi-logarithmic scale in the absence and presence of a magnetic field.

The corresponding PL decay curves were taken for 389 nm and 468 nm of color centers in presence and absence of magnetic field (Figure 31a and b).

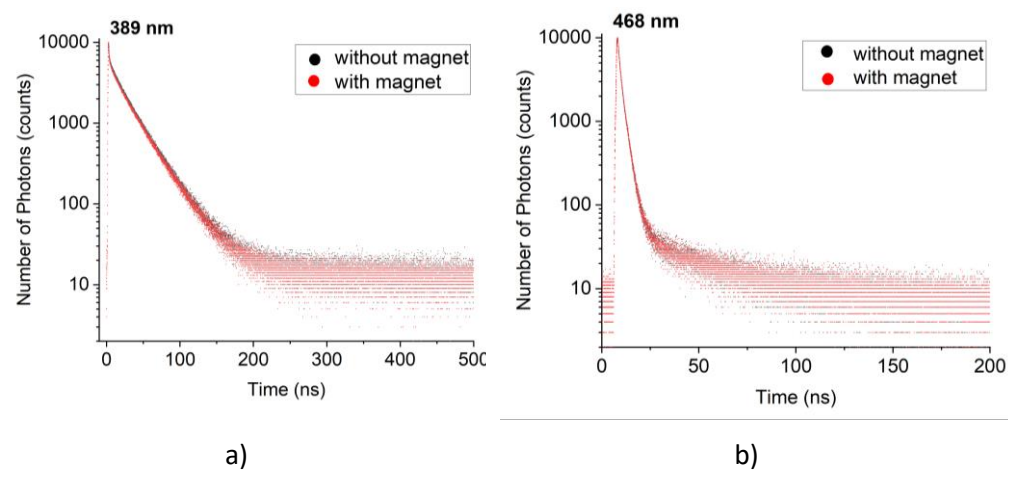


Figure 31. PL decay curves for a) – 389 nm color center and b) – 468 nm color center on a semi-logarithmic scale in the absence and presence of a magnetic field.

Table 5 summarizes the fitting results of the NV⁻ PL decay curves, showing the retrieved lifetime components together with their corresponding amplitude. The fitting error does not exceed 2%.

Magnetic field	A ₁	t ₁ ,	\mathbf{A}_{2}^{\prime}	t ₂ , ns	F ₂ '	\mathbf{A}_3'	t ₃ , ns	F ₃ '	t _{avg} , ns
Absent	0,846	1,83	0,909	6,14	0,820	0,091	13,52	0,180	6,81
Present	0,954	1,31	0,412	5,67	0,267	0,588	10,92	0,733	8,76

Table 5. The results of NV color center PL decay curves fitting.

From Table 5, it can be seen that with the presence of a magnetic field, the long PL lifetime component (t_3) undergoes a 19% decrease, while the short one (t_2) demonstrates a less substantial reduction of about 8%. However, the multi-exponential tail fits can exhibit coupling between amplitudes (A_i) and lifetimes (t_i) , and thus the changes in fitted lifetime components are better interpreted together with their amplitudes for a more reliable comparison of the retrieved data. Therefore, the amplitude-weighted mean lifetimes (t_{avg}) and integrated photon fractions (F_i) were also reported.

The amplitude-weighted mean lifetime is defined according to expression:

$$t_{avg} = \frac{\sum_{i} A_i t_i}{\sum_{i} A_i} \tag{11}$$

and gives an effective average decay time, accounting for the relative contribution of each exponential component.

The Integrated photon fraction is defined according to expression:

$$F_i = \frac{A_i t_i}{\sum_i A_i t_i} \tag{12}$$

and represents the relative share of emitted photons associated with the corresponding decay channel.

It should be noted that the amplitude-weighted mean lifetimes and integrated photon fractions in this part of the work were calculated by considering only the short and long lifetime components together with their corresponding amplitudes, while excluding the fast lifetime component, since it is mainly related to the present setup and the IRF function and does not represent a physical lifetime component associated with the PL dynamics of the color centers.

From these additional values it could be seen that the integrated photon fraction of the short component decreases considerably under the magnetic field (from \sim 0.82 to \sim 0.27). At the same time, the long component exhibits a pronounced increase in its integrated photon fraction (from \sim 0.18 to \sim 0.73). The amplitude-weighted average lifetime increases from \sim 6.8 ns to \sim 8.8 ns in the presence of the magnetic field, which may indicate a redistribution of the PL decay dynamics toward long lifetime channel under magnetic field influence.

Table 6 summarizes the fitting results of the 389 nm PL decay curves, showing the retrieved lifetime components together with their corresponding amplitudes,

integrated photon fractions, and the amplitude-weighted average lifetime. The fitting error does not exceed 2%.

Magnetic field	A ₁	t ₁ , ns	$\mathbf{A_2'}$	t ₂ , ns	F_2'	\mathbf{A}_3'	t₃, ns	F_3'	t _{avg} , ns
Absent	0,988	0,6	0,333	8,7	0,131	0,667	28,8	0,869	22,10
Present	0,995	0,5	0,250	6,8	0,074	0,750	28,3	0,926	22,95

Table 6. The results of 389 nm color center PL decay curves fitting.

From Table 6, it can be seen that, in the presence of a magnetic field, the long PL lifetime component (t_3) undergoes only a minor decrease of about 2%, while the short component (t_2) shows a much more pronounced reduction of ~20%. However, the amplitude-weighted average lifetime exhibits a subtle increase, as was also observed for NV $^-$ color center, that again could point out on a redistribution of the PL decay dynamics toward long lifetime channel under magnetic field influence.

Table 7 summarizes the fitting results of the 468 nm PL decay curves, showing the retrieved lifetime components together with their corresponding amplitudes. The fitting error does not exceed 2%.

Magnetic field	A ₁	t ₁ , ns	\mathbf{A}_2'	t ₂ , ns
Absent	0,996	1,05	1	3,06
Present	0,997	1,01	1	2,94

Table 7. The results of 468 nm color center PL decay curves fitting.

Table 7 demonstrates that both the fast and short lifetime components undergo a ~4% decrease in the presence of a magnetic field, suggesting that the 468 nm color center exhibits an overall subtle sensitivity to the applied magnetic field in its PL decay dynamics.

Summing up the analysis of the presented data, it can be concluded that the 389 nm and 468 nm color centers, by demonstrating changes in their PL decay dynamics, could potentially be utilized for all-optical magnetometry, with the 389 nm center appearing more sensitive due to pronounced sensitivity of its short-lifetime component behavior.

To sum up the section on all-optical magnetometry with the 389 nm and 468 nm color centers, it can be concluded that this proof-of-concept study confirmed the feasibility of sensing through PL intensity quenching and changes in lifetime component dynamics. The observed results are also of great interest from the fundamental study point of view, since they point to a possible splitting of energy states in the level structure of these defects. Further investigation will be directed toward systematic variation of magnetic-field values, as well as DFT calculations, to clarify the origin of the observed effect.

4.4 Influence of methane concentration during CVD growth on NV charge state

This section presents the results of evaluating the relative concentrations of NV^- and NV^0 color centers in studied SCDNs samples synthesized under varying methane concentrations (1,6% to 5,3%), as summarized in Table 8.

Number of Sample	364	369	371	379	382	387
CH ₄ ,%	5,3	4,6	3,9	3,1	2,3	1,6

Table 8. Methane concentration for PE-CVD growth of the SCDNs samples.

The pipeline employing the NNMF approach for spectral decomposition, followed by applying the retrieved component contributions to saturation values for concentration estimation, is comprehensively described in the Methods and materials section. Therefore, this section focuses only on presenting the estimated concentrations of NV⁻ and NV⁰ color centers.

Table 9 presents the saturation intensities obtained for the NV⁻ ensembles, together with the ratio of these values to the saturation intensity of a single NV⁻ center, calculated as 561398 a.u. This ratio provides an estimate of the number of NV⁻ centers within the confocal collection volume. Since the collection volume is known (\approx 0,29 μ m³ for an excitation wavelength of 700 nm and objective NA = 1,35), the NV⁻ concentration can be determined and expressed in cm⁻³. To further convert the obtained concentration into parts per billion (ppb), equation (13) was applied.

$$C_{NV}[ppb] = \frac{C_{NV}[cm^{-3}]}{1.77 * 10^{14}}$$
 (13)

where C_{NV} – color center concentration in cm $^{\text{-}3}$. Both concentrations are presented in Table 9.

CH ₄ , %	Isat_ensemble, a.u.	N _{NV}	C _{NV} , cm ⁻³	C _{NV} , ppb
5,3	19075010	33,97	1,17·10 ¹⁴	0,66
4,6	53165827	94,70	3,27·10 ¹⁴	1,84
3,9	50050656	89,15	3,07·10 ¹⁴	1,74
3,1	58524611	104,25	3,59·10 ¹⁴	2,03
2,3	33991458	60,55	2,09·10 ¹⁴	1,18
1,6	45307130	80,70	2,78·10 ¹⁴	1,57

Table 9. Calculation of NV⁻ concentration from saturation intensities and the resulting values.

The corresponding data for the NV 0 color center concentration are presented in Table 10. For this calculation, owing to the different emission wavelength (599 nm), the confocal collection volume was taken as 0,17 μ m 3 . Due to the absence of a sample with a single NV 0 color center to measure its power vs. intensity curve followed by calculation, the calculation of saturation intensity for a single NV 0 center was conducted using relation (14):

$$I_{sat}(NV^0) = k * I_{sat}(NV^-)$$
(14)

where k is determined according to expression (15):

$$k = \frac{\tau_{NV} - \sigma_{NV}}{\tau_{NV0} \sigma_{NV0}} \tag{15}$$

in which σ_{NV-} and σ_{NV0} are absorption cross sections of corresponding color centers and τ_{NV-} and τ_{NV0} – PL decay times. For k calculations, the values were taken from [32,91], and the saturation intensity of a single NV 0 center was calculated as 142922 a.u.

Figure 32 illustrates the dependence of NV⁻ and NV⁰ color center concentrations on methane concentration during CVD growth of SCDNs, with corresponding uncertainty ribbons included to reflect the reliability of the extracted value.

CH ₄ ,%	I _{sat_ensemble} , a.u.	N _{NV}	C _{NV} , cm ⁻³	ppb
5,3	884139	6,19	3,64·10 ¹³	021
4,6	705078	4,93	2,90·10 ¹³	0,16
3,9	123824	0,87	5,10·10 ¹²	0,03
3,1	159712	1,12	6,57·10 ¹²	0,04
2,3	50745	0,36	2,09·10 ¹²	0,01
1,6	221721	1,55	9,13·10 ¹²	0,05

Table 10. Calculation of NV^0 concentration from saturation intensities and the resulting values.

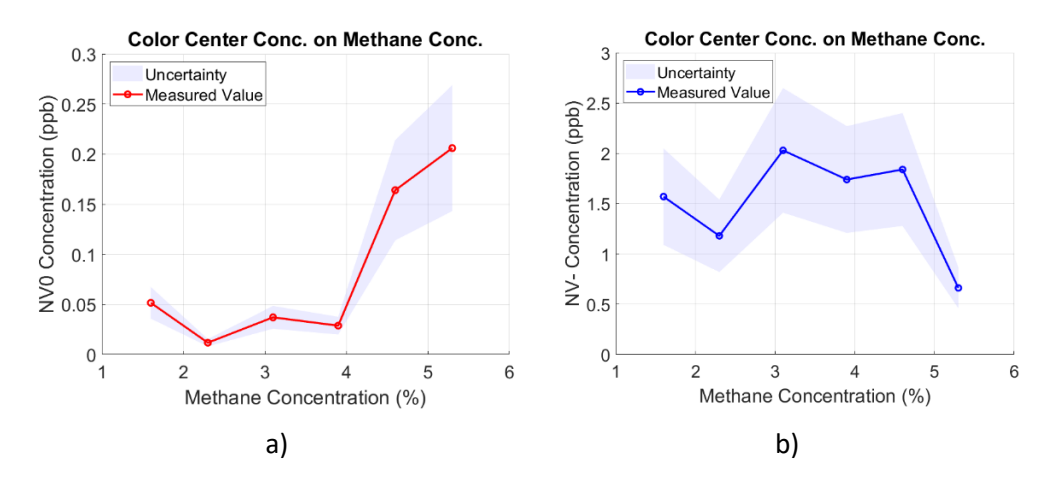


Figure 32. The dependences on methane concentration of a) - NV 0 color center concentration and b) NV $^{-}$ color center concentration.

For better understanding of methane concentration influence on NV⁻/NV⁰ color center formation, the ratio between NV⁻ and NV⁰ color center concentrations were found and plotted against methane concentration values (Figure 33).

An obtained plot demonstrates a clear non-monotonic trend in which the ratio reaches its maximum around 2,3% CH₄, pointing out on a domination of the negatively charged state (NV⁻). For concentration 1,6% and intermediate concentrations (3,0–4,0%), the NV⁻/NV⁰ ratio remains relatively high, whereas at higher CH₄ content (>4,5%) a sharp decrease of the ratio is observed, indicating preferential formation of the neutral state (NV⁰).

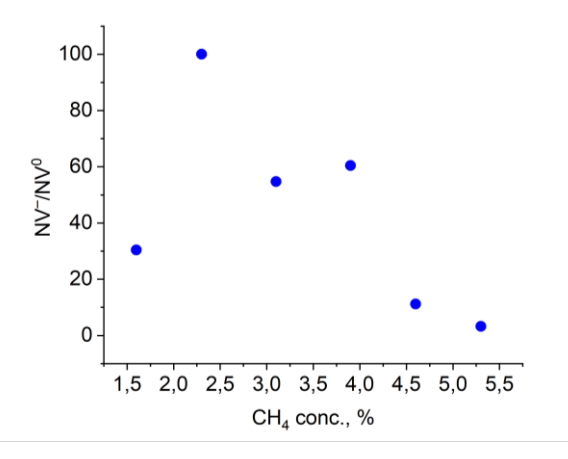


Figure 33. NV⁻/NV⁰ concentrations ratio vs. methane concentration in studied samples.

Therefore, the conducted analysis allowed to understand the overall influence of methane concentration used during the SCDNs CVD growth on NV charge state, as well as resulting in the determination of methane concentration windows favoring NV 0 and NV $^{-}$ color centers formation, crucial for developing SCDNs-based quantum sensing platforms.

Conclusion

This work has reviewed the current achievements and challenges in the field of quantum sensing with color centers, specifically in the all-optical diamond platform. It was revealed that most of the progress is related to the NV⁻ center, with the SiV⁻ center also gaining momentum. However, the potential of other centers, such as the 389 nm and 468 nm centers, remains overshadowed, although they could provide a solution for expanding the operational wavelength range of diamond-based quantum sensing platforms, and in particular, of single-crystal diamond needles studied in this work.

The study revealed six distinct color centers in the investigated samples, with the 389 nm, 468 nm, and NVO centers consistently present. It was demonstrated that the gas composition used during chemical vapor deposition growth plays a crucial role in color center formation and can be applied as a strong tool for controlled defect engineering. In particular, methane-rich growth conditions suppressed the 389 nm center, whereas nitrogen addition shifted the balance of NV charge states toward NV⁻.

Beyond spectral characterization, this thesis demonstrated a proof-of-concept of all-optical sensing with the 389 nm and 468 nm centers. Both centers exhibited temperature-dependent shifts of their zero-phonon lines, and in the case of the 468 nm center, an additional change in the zero-phonon line-to-3rd phonon replica ratio was observed, providing an alternative sensing parameter. Although the extracted temperature resolutions (8,3 K and 2,2 K in the biological temperature range) are above the state-of-the-art values, the analysis performed in this work suggests that with optimized instrumentation and improved uncertainty evaluation, these centers could reach sub-kelvin sensitivity. Magnetometry experiments further indicated that photoluminescence quenching and lifetime dynamics of the 389 nm and 468 nm centers are sensitive to magnetic fields, which highlights their potential for future quantum sensing applications.

This thesis also presented the development of a pipeline for photoluminescence spectra decomposition, based on non-negative matrix factorization. This method was successfully applied to evaluate the concentrations of NV⁻ and NV⁰ centers in samples grown with different methane concentrations. The resulting analysis of NV charge states allowed the determination of methane concentration windows favoring the formation of either NV⁰ or NV⁻ centers, which is crucial for the development of single-crystal diamond needle-based quantum sensing platforms.

Future research should focus on systematic magnetic field variation, improvement of spectral resolution, and theoretical modeling, such as density functional theory calculations, to clarify the energy level structure of the 389 nm and 468 nm defects. Such studies will also possibly allow for optimizing their integration into diamond-based quantum sensing platforms.

References

- [1] J.E. Field, ed., *The properties of natural and synthetic diamond*, London [u.a.]: Academic Press, 1992.
- [2] G. Davies, "The Jahn-Teller effect and vibronic coupling at deep levels in diamond," *Reports on Progress in Physics*, vol. 44, Jul. 1981, pp. 787–830.
- [3] L. Wei, P.K. Kuo, R.L. Thomas, T.R. Anthony, and W.F. Banholzer, "Thermal conductivity of isotopically modified single crystal diamond," *Physical Review Letters*, vol. 70, Jun. 1993, pp. 3764–3767.
- [4] J. Isberg, J. Hammersberg, E. Johansson, T. Wikström, D.J. Twitchen, A.J. Whitehead, S.E. Coe, and G.A. Scarsbrook, "High Carrier Mobility in Single-Crystal Plasma-Deposited Diamond," *Science*, vol. 297, Sep. 2002, pp. 1670–1672.
- [5] O. Auciello, P. Gurman, M.B. Guglielmotti, D.G. Olmedo, A. Berra, and M.J. Saravia, "Biocompatible ultrananocrystalline diamond coatings for implantable medical devices," *MRS Bulletin*, vol. 39, Jul. 2014, pp. 621–629.
- [6] X. Xiao, J. Wang, C. Liu, J.A. Carlisle, B. Mech, R. Greenberg, D. Guven, R. Freda, M.S. Humayun, J. Weiland, and O. Auciello, "In vitro and in vivo evaluation of ultrananocrystalline diamond for coating of implantable retinal microchips," *Journal of Biomedical Materials Research Part B: Applied Biomaterials*, vol. 77B, Oct. 2005, pp. 273–281.
- [7] W. Kaiser and W.L. Bond, "Nitrogen, A Major Impurity in Common Type I Diamond," *Physical Review*, vol. 115, Aug. 1959, pp. 857–863.
- [8] L.D. Preez, "Electron paramagnetic resonance and optical investigations of defect centres in diamond," University of the Witwatersrand, Johannesburg, 1965.
- [9] F.P. Bundy, H.T. Hall, H.M. Strong, and R.H. Wentorfjun., "Man-Made Diamonds," *Nature*, vol. 176, Jul. 1955, pp. 51–55.
- [10] J.C. Angus, H.A. Will, and W.S. Stanko, "Growth of Diamond Seed Crystals by Vapor Deposition," *Journal of Applied Physics*, vol. 39, May. 1968, pp. 2915–2922.
- [11] A. Gruber, A. Dräbenstedt, C. Tietz, L. Fleury, J. Wrachtrup, and C. von Borczyskowski, "Scanning Confocal Optical Microscopy and Magnetic Resonance on Single Defect Centers," *Science*, vol. 276, Jun. 1997, pp. 2012–2014.
- [12] F. Jelezko and J. Wrachtrup, "Read-out of single spins by optical spectroscopy," *Journal of Physics: Condensed Matter*, vol. 16, Jul. 2004, pp. R1089–R1104.
- [13] F. Jelezko, T. Gaebel, I. Popa, A. Gruber, and J. Wrachtrup, "Observation of Coherent Oscillations in a Single Electron Spin," *Physical Review Letters*, vol. 92, Feb. 2004, p. 076401.
- [14] G. Balasubramanian, I.Y. Chan, R. Kolesov, M. Al-Hmoud, J. Tisler, C. Shin, C. Kim, A. Wojcik, P.R. Hemmer, A. Krueger, T. Hanke, A. Leitenstorfer, R. Bratschitsch, F. Jelezko, and J. Wrachtrup, "Nanoscale imaging magnetometry with diamond spins under ambient conditions," *Nature*, vol. 455, Oct. 2008, pp. 648–651.
- [15] P. Maletinsky, S. Hong, M.S. Grinolds, B. Hausmann, M.D. Lukin, R.L. Walsworth, M. Loncar, and A. Yacoby, "A robust scanning diamond sensor for nanoscale imaging with single nitrogen-vacancy centres," *Nature Nanotechnology*, vol. 7, Apr. 2012, pp. 320–324.
- [16] A.O. Sushkov, N. Chisholm, I. Lovchinsky, M. Kubo, P.K. Lo, S.D. Bennett, D. Hunger, A. Akimov, R.L. Walsworth, H. Park, and M.D. Lukin, "All-Optical Sensing of a Single-Molecule Electron Spin," *Nano Letters*, vol. 14, Oct. 2014, pp. 6443–6448.

- [17] "Diamond nitrogen vacancy sensor with circuitry on diamond," U.S. Patent US9823313B2, 2016.
- [18] A.Y. Sungkun Hong Patrick Maletinsky Michael S. Grinolds, "Nanoscale scanning sensors," U.S. Patent WO2014051886A1, 2013.
- [19] M.P. J. Cai F. Jelezko, "Sensor comprising a piezomagnetic or piezoelectric element on a diamond substrate with a colour centre," U.S. Patent EP3132278B1, 2014.
- [20] T. Zhang, G. Pramanik, K. Zhang, M. Gulka, L. Wang, J. Jing, F. Xu, Z. Li, Q. Wei, P. Cigler, and Z. Chu, "Toward Quantitative Bio-sensing with Nitrogen–Vacancy Center in Diamond," *ACS Sensors*, vol. 6, May. 2021, pp. 2077–2107.
- [21] M. Quarshie, L. Golubewa, C. Giraulo, S. Morello, C. Cirillo, M. Sarno, B. Xu, P. Balasubramanian, Y. Mindarava, M. Tutkus, A. Obraztsov, F. Jelezko, P. Kuzhir, and S. Malykhin, "Diamond nanoneedles for biosensing," *Nanotechnology*, vol. 36, Mar. 2025, p. 165501.
- [22] D. Rani, O. Opaluch, and E. Neu, "Recent Advances in Single Crystal Diamond Device Fabrication for Photonics, Sensing and Nanomechanics," *Micromachines*, vol. 12, Dec. 2020, p. 36.
- [23] Y. Li, X. Zhu, H. Zhang, Y. Lu, T. Zeng, H. Liu, T. Li, J. Wang, and L. Tang, "Nanodiamond in cancer theranostics," *Nano TransMed*, vol. 2, Mar. 2023, p. e9130019.
- [24] Y. Wu, F. Jelezko, M.B. Plenio, and T. Weil, "Diamond Quantum Devices in Biology," *Angewandte Chemie International Edition*, vol. 55, Apr. 2016, pp. 6586–6598.
- [25] I. Panadero, H. Espinós, L. Tsunaki, K. Volkova, A. Tobalina, J. Casanova, P. Acedo, B. Naydenov, R. Puebla, and E. Torrontegui, "Photon-emission statistics for single nitrogen-vacancy centers," *Physical Review Applied*, vol. 22, Jul. 2024, p. 014035.
- [26] A. Dementjev, R. Karpicz, B. Xu, S. Malykhin, Y. Svirko, and P. Kuzhir, "Polarization CARS microscopy of diamond needles," *Applied Physics Letters*, vol. 124, May. 2024.
- [27] R. Ismagilov, S. Malykhin, A. Puzyr, A. Loginov, V. Kleshch, and A. Obraztsov, "Single-Crystal Diamond Needle Fabrication Using Hot-Filament Chemical Vapor Deposition," *Materials*, vol. 14, Apr. 2021, p. 2320.
- [28] S.A. Malykhin, R.R. Ismagilov, F.T. Tuyakova, E.A. Obraztsova, P.V. Fedotov, A. Ermakova, P. Siyushev, K.G. Katamadze, F. Jelezko, Y.P. Rakovich, and A.N. Obraztsov, "Photoluminescent properties of single crystal diamond microneedles," *Optical Materials*, vol. 75, Jan. 2018, pp. 49–55.
- [29] M.W.N. Ngambou, C. Pellet-Mary, O. Brinza, A. Antonino, G. Hetet, A. Tallaire, F. Bénédic, and J. Achard, "Improving NV centre density during diamond growth by CVD process using N2O gas," *Diamond and Related Materials*, vol. 123, Mar. 2022, p. 108884.
- [30] T. Teraji, C. Shinei, Y. Masuyama, M. Miyakawa, and T. Taniguchi, "Nitrogen concentration control during diamond growth for NV centre formation," *Philosophical Transactions of the Royal Society A: Mathematical, Physical and Engineering Sciences*, vol. 382, Dec. 2023.
- [31] A. Zaitsev, Optical properties of diamond, Berlin: Springer, 2001.
- [32] E. Filonenko, P. Kuzhir, and S. Malykhin, "Fluorescence dynamics of color centers in diamond needles," *Nanotechnology*, vol. 36, Apr. 2025, p. 185702.
- [33] S. Malykhin, Y. Mindarava, R. Ismagilov, F. Jelezko, and A. Obraztsov, "Control of NV, SiV and GeV centers formation in single crystal diamond needles," *Diamond and Related Materials*, vol. 125, May. 2022, p. 109007.

- [34] S. Malykhin, Y. Mindarava, R. Ismagilov, A. Orekhov, F. Jelezko, and A. Obraztsov, "Formation of GeV, SiV, and NV Color Centers in Single Crystal Diamond Needles Grown by Chemical Vapor Deposition," *physica status solidi* (b), vol. 256, Mar. 2019.
- [35] L. Horsthemke, J. Pogorzelski, D. Stiegekötter, F. Hoffmann, L. Langguth, R. Staacke, C. Laube, W. Knolle, M. Gregor, and P. Glösekötter, "Excited-State Lifetime of NV Centers for All-Optical Magnetic Field Sensing," *Sensors*, vol. 24, Mar. 2024, p. 2093.
- [36] S. Häußler, G. Thiering, A. Dietrich, N. Waasem, T. Teraji, J. Isoya, T. Iwasaki, M. Hatano, F. Jelezko, A. Gali, and A. Kubanek, "Photoluminescence excitation spectroscopy of SiV–and GeV–color center in diamond," *New Journal of Physics*, vol. 19, Jun. 2017, p. 063036.
- [37] E.A. Ekimov, P.S. Sherin, V.S. Krivobok, S.G. Lyapin, V.A. Gavva, and M.V. Kondrin, "Photoluminescence excitation study of split-vacancy centers in diamond," *Physical Review B*, vol. 97, Jan. 2018, p. 045206.
- [38] L. Golubewa, Y. Padrez, S. Malykhin, T. Kulahava, E. Shamova, I. Timoshchenko, M. Franckevicius, A. Selskis, R. Karpicz, A. Obraztsov, Y. Svirko, and P. Kuzhir, "All-Optical Thermometry with NV and SiV Color Centers in Biocompatible Diamond Microneedles," *Advanced Optical Materials*, vol. 10, May. 2022.
- [39] N.B. Manson, K. Beha, A. Batalov, L.J. Rogers, M.W. Doherty, R. Bratschitsch, and A. Leitenstorfer, "Assignment of the NV0575-nm zero-phonon line in diamond to a2E-2A2transition," *Physical Review B*, vol. 87, Apr. 2013, p. 155209.
- [40] M.W. Doherty, N.B. Manson, P. Delaney, F. Jelezko, J. Wrachtrup, and L.C.L. Hollenberg, "The nitrogen-vacancy colour centre in diamond," *Physics Reports*, vol. 528, Jul. 2013, pp. 1–45.
- [41] A. Pershin, A. Tárkányi, V. Verkhovlyuk, V. Ivády, and A. Gali, "A Coherence-Protection Scheme for Quantum Sensors Based on Ultra-Shallow Single Nitrogen-Vacancy Centers in Diamond," 2025.
- [42] G. Bayer, R. Berghaus, S. Sachero, A.B. Filipovski, L. Antoniuk, N. Lettner, R. Waltrich, M. Klotz, P. Maier, V. Agafonov, and A. Kubanek, "Optical driving, spin initialization and readout of single SiV– centers in a Fabry-Perot resonator," *Communications Physics*, vol. 6, Oct. 2023.
- [43] C. Chen, B. Jiang, and X. Hu, "Research Progress on Silicon Vacancy Color Centers in Diamond," *Functional Diamond*, vol. 4, Mar. 2024.
- [44] L. Venturi, L. Rigutti, J. Houard, I. Blum, S. Malykhin, A. Obraztsov, and A. Vella, "Strain sensitivity and symmetry of 2.65 eV color center in diamond nanoscale needles," *Applied Physics Letters*, vol. 114, Apr. 2019.
- [45] S.A. Malykhin, J. Houard, R.R. Ismagilov, A.S. Orekhov, A. Vella, and A.N. Obraztsov, "Luminescent Characteristics of Needle-Like Single Crystal Diamonds," *physica status solidi (b)*, vol. 255, Oct. 2017.
- [46] R.G. Burns, *Mineralogical Applications of Crystal Field Theory*, Cambridge University Press, 1993.
- [47] R. Katsumi, K. Takada, F. Jelezko, and T. Yatsui, "Recent progress in hybrid diamond photonics for quantum information processing and sensing," *Communications Engineering*, vol. 4, May. 2025.
- [48] G. Thiering and A. Gali, "Color centers in diamond for quantum applications," *Diamond for Quantum Applications Part 1*, Elsevier, 2020, pp. 1–36.
- [49] S.D. Subedi, V.V. Fedorov, J. Peppers, D.V. Martyshkin, S.B. Mirov, L. Shao, and M. Loncar, "Laser spectroscopic characterization of negatively charged nitrogen-vacancy (NV-)

- centers in diamond," Optical Materials Express, vol. 9, Apr. 2019, p. 2076.
- [50] A. Dietrich, K.D. Jahnke, J.M. Binder, T. Teraji, J. Isoya, L.J. Rogers, and F. Jelezko, "Isotopically varying spectral features of silicon-vacancy in diamond," *New Journal of Physics*, vol. 16, Nov. 2014, p. 113019.
- [51] L.J. Rogers, K.D. Jahnke, M.H. Metsch, A. Sipahigil, J.M. Binder, T. Teraji, H. Sumiya, J. Isoya, M.D. Lukin, P. Hemmer, and F. Jelezko, "All-Optical Initialization, Readout, and Coherent Preparation of Single Silicon-Vacancy Spins in Diamond," *Physical Review Letters*, vol. 113, Dec. 2014, p. 263602.
- [52] A. Sipahigil, K.D. Jahnke, L.J. Rogers, T. Teraji, J. Isoya, A.S. Zibrov, F. Jelezko, and M.D. Lukin, "Indistinguishable Photons from Separated Silicon-Vacancy Centers in Diamond," *Physical Review Letters*, vol. 113, Sep. 2014, p. 113602.
- [53] M. Fujiwara, G. Uchida, I. Ohki, M. Liu, A. Tsurui, T. Yoshikawa, M. Nishikawa, and N. Mizuochi, "All-optical nanoscale thermometry based on silicon-vacancy centers in detonation nanodiamonds," *Carbon*, vol. 198, Oct. 2022, pp. 57–62.
- [54] G. Thiering and A. Gali, "Ab Initio Magneto-Optical Spectrum of Group-IV Vacancy Color Centers in Diamond," *Physical Review X*, vol. 8, Jun. 2018, p. 021063.
- [55] C. Hepp, T. Müller, V. Waselowski, J.N. Becker, B. Pingault, H. Sternschulte, D. Steinmüller-Nethl, A. Gali, J.R. Maze, M. Atatüre, and C. Becher, "Electronic Structure of the Silicon Vacancy Color Center in Diamond," *Physical Review Letters*, vol. 112, Jan. 2014, p. 036405.
- [56] A.T. Collins, M. Kamo, and Y. Sato, "Optical centres related to nitrogen, vacancies and interstitials in polycrystalline diamond films grown by plasma-assisted chemical vapour deposition," *Journal of Physics D: Applied Physics*, vol. 22, Sep. 1989, pp. 1402–1405.
- [57] A.T. Collins, P.J. Woad, G.S. Woods, and H. Kanda, "Localised vibrational modes in diamonds grown from mixed carbon isotopes," *Diamond and Related Materials*, vol. 2, Mar. 1993, pp. 136–141.
- [58] K. Iakoubovskii and G.J. Adriaenssens, "Luminescence excitation spectra in diamond," *Physical Review B*, vol. 61, Apr. 2000, pp. 10174–10182.
- [59] J. Ruan, W.J. Choyke, and W.D. Partlow, "Cathodoluminescence and annealing study of plasma-deposited polycrystalline diamond films," *Journal of Applied Physics*, vol. 69, May. 1991, pp. 6632–6636.
- [60] M. Mansoor, K. Czelej, S. Eaton-Magaña, M. Mansoor, R. Salci, M. Mansoor, T. Linzmeyer, Y. Sorkhe, K.S. Moe, Ö. Özyildirim, K. Kitajima, M.A. Sarsil, T. Erol, G. Hamamci, O. Ergen, A. Kurt, A.A. Akhavan, Z. Er, S. Rubanov, N.M. Kazuchits, A. Gokce, N. Davies, S. Timur, S. Prawer, A. Zaitsev, and M. Ürgen, "Engineering NV Centers via Hydrogen-Driven Defect Chemistry in CVD Diamonds for Quantum Applications: NVHx Dissociations into NV, Origin of 468nm Center, and Cause of Brown Coloration," 2025.
- [61] K.A. Abdelghafar, D.S. Choi, and K. Askar, "Modelling of blue luminescent color centers in brown diamond: A density functional theory study," *Diamond and Related Materials*, vol. 158, Oct. 2025, p. 112655.
- [62] A.N. Obraztsov, A.A. Zolotukhin, A.O. Ustinov, A.P. Volkov, and Y.P. Svirko, "Chemical vapor deposition of carbon films: in-situ plasma diagnostics," *Carbon*, vol. 41, 2003, pp. 836–839.
- [63] A.M. Edmonds, U.F.S. D'Haenens-Johansson, R.J. Cruddace, M.E. Newton, K.-M.C. Fu, C. Santori, R.G. Beausoleil, D.J. Twitchen, and M.L. Markham, "Production of oriented nitrogen-

- vacancy color centers in synthetic diamond," Physical Review B, vol. 86, Jul. 2012, p. 035201.
- [64] C.J. Tang, A.J.S. Fernandes, X.F. Jiang, J.L. Pinto, and H. Ye, "Effect of methane concentration in hydrogen plasma on hydrogen impurity incorporation in thick large-grained polycrystalline diamond films," *Journal of Crystal Growth*, vol. 426, Sep. 2015, pp. 221–227.
- [65] D.B. Radishev, M.A. Lobaev, S.A. Bogdanov, A.M. Gorbachev, A.L. Vikharev, and M.N. Drozdov, "Investigation of NV centers charge states in CVD diamond layers doped by nitrogen and phosphorous," *Journal of Luminescence*, vol. 239, Nov. 2021, p. 118404.
- [66] T. Luo, L. Lindner, J. Langer, V. Cimalla, X. Vidal, F. Hahl, C. Schreyvogel, S. Onoda, S. Ishii, T. Ohshima, D. Wang, D.A. Simpson, B.C. Johnson, M. Capelli, R. Blinder, and J. Jeske, "Creation of nitrogen-vacancy centers in chemical vapor deposition diamond for sensing applications," *New Journal of Physics*, vol. 24, Mar. 2022, p. 033030.
- [67] R. Hanson, O. Gywat, and D.D. Awschalom, "Room-temperature manipulation and decoherence of a single spin in diamond," *Physical Review B*, vol. 74, Oct. 2006, p. 161203.
- [68] E. Bauch, S. Singh, J. Lee, C.A. Hart, J.M. Schloss, M.J. Turner, J.F. Barry, L.M. Pham, N. Bar-Gill, S.F. Yelin, and R.L. Walsworth, "Decoherence of ensembles of nitrogen-vacancy centers in diamond," *Physical Review B*, vol. 102, Oct. 2020, p. 134210.
- [69] M.A. Lobaev, A.M. Gorbachev, S.A. Bogdanov, A.L. Vikharev, D.B. Radishev, V.A. Isaev, and M.N. Drozdov, "NV-Center Formation in Single Crystal Diamond at Different CVD Growth Conditions," *physica status solidi (a)*, vol. 215, Sep. 2018.
- [70] S. Esmaeili, P. Schmalenberg, S. Wu, Y. Zhou, S. Rodrigues, N. Hussain, T. Kimura, Y. Tadokoro, S. Higashi, D. Banerjee, and E.M. Dede, "Evolution of quantum spin sensing: From bench-scale ODMR to compact integrations," *APL Materials*, vol. 12, Apr. 2024.
- [71] B. Bürgler, T.F. Sjolander, O. Brinza, A. Tallaire, J. Achard, and P. Maletinsky, "All-optical nuclear quantum sensing using nitrogen-vacancy centers in diamond," *npj Quantum Information*, vol. 9, Jun. 2023.
- [72] Y. Zhu, E. Losero, C. Galland, and V. Goblot, "Simulation of ODMR Spectra from Nitrogen-Vacancy Ensembles in Diamond for Electric Field Sensing," 2023.
- [73] M.S. Alam, F. Gorrini, M. Gawełczyk, D. Wigger, G. Coccia, Y. Guo, S. Shahbazi, V. Bharadwaj, A. Kubanek, R. Ramponi, P.E. Barclay, A.J. Bennett, J.P. Hadden, A. Bifone, S.M. Eaton, and P. Machnikowski, "Determining strain components in a diamond waveguide from zero-field optically detected magnetic resonance spectra of negatively charged nitrogen-vacancy-center ensembles," *Physical Review Applied*, vol. 22, Aug. 2024, p. 024055.
- [74] V.M. Acosta, E. Bauch, M.P. Ledbetter, A. Waxman, L.S. Bouchard, and D. Budker, "Temperature dependence of the nitrogen-vacancy magnetic resonance in diamond," 2009.
- [75] M.C. Cambria, G. Thiering, A. Norambuena, H.T. Dinani, A. Gardill, I. Kemeny, V. Lordi, Á. Gali, J.R. Maze, and S. Kolkowitz, "Physically motivated analytical expression for the temperature dependence of the zero-field splitting of the nitrogen-vacancy center in diamond," *Physical Review B*, vol. 108, Nov. 2023, p. 1180102.
- [76] V. Ivády, T. Simon, J.R. Maze, I.A. Abrikosov, and A. Gali, "Pressure and temperature dependence of the zero-field splitting in the ground state of NV centers in diamond: A first-principles study," *Physical Review B*, vol. 90, Dec. 2014, p. 235205.
- [77] N. Sekiguchi, M. Fushimi, A. Yoshimura, C. Shinei, M. Miyakawa, T. Taniguchi, T. Teraji, H. Abe, S. Onoda, T. Ohshima, M. Hatano, M. Sekino, and T. Iwasaki, "Diamond quantum magnetometer with dc sensitivity of sub-10 pT Hz–1/2 toward measurement of biomagnetic field," *Physical Review Applied*, vol. 21, Jun. 2024, p. 064010.

- [78] J.-P. Tetienne, L. Rondin, P. Spinicelli, M. Chipaux, T. Debuisschert, J.-F. Roch, and V. Jacques, "Magnetic-field-dependent photodynamics of single NV defects in diamond: Application to qualitative all-optical magnetic imaging," 2012.
- [79] M.W. Doherty, V.M. Acosta, A. Jarmola, M.S.J. Barson, N.B. Manson, D. Budker, and L.C.L. Hollenberg, "Temperature shifts of the resonances of the NV-center in diamond," *Physical Review B*, vol. 90, Jul. 2014, p. 041201.
- [80] P. Balasubramanian, M.H. Metsch, P. Reddy, L.J. Rogers, N.B. Manson, M.W. Doherty, and F. Jelezko, "Discovery of ST1 centers in natural diamond," *Nanophotonics*, vol. 8, Aug. 2019, pp. 1993–2002.
- [81] J. Foglszinger, A. Denisenko, T. Kornher, M. Schreck, W. Knolle, B. Yavkin, R. Kolesov, and J. Wrachtrup, "TR12 centers in diamond as a room temperature atomic scale vector magnetometer," *npj Quantum Information*, vol. 8, Jun. 2022.
- [82] J. Foglszinger, A. Denisenko, G.V. Astakhov, L. Kazak, P. Siyushev, A.M. Zaitsev, R. Kolesov, and J. Wrachtrup, "Discovery of ST2 centers in natural and CVD diamond," 2025.
- [83] P.G. Kopylov, A.N. Obraztsov, and P.V. Shvets, "Formation of needlelike crystallites during growth of diamond films by chemical vapor deposition," *Crystallography Reports*, vol. 55, Jul. 2010, pp. 710–715.
- [84] J.R. Lakowicz, *Principles of fluorescence spectroscopy*, New York, NY: Springer, 2010.
- [85] D.M. Jameson, Introduction to Fluorescence, CRC Press, 2014.
- [86] I. Panadero, H. Espinós, L. Tsunaki, K. Volkova, A. Tobalina, J. Casanova, P. Acedo, B. Naydenov, R. Puebla, and E. Torrontegui, "Characterization of the photon emission statistics in nitrogen-vacancy centers," 2023.
- [87] W. Liu, N. Zheng, and Q. You, "Nonnegative matrix factorization and its applications in pattern recognition," *Chinese Science Bulletin*, vol. 51, Jan. 2006, pp. 7–18.
- [88] G. Thalassinos, D.J. McCloskey, A. Mameli, A.J. Healey, C. Pattinson, D. Simpson, B.C. Gibson, A. Stacey, N. Dontschuk, and P. Reineck, "Robust quantification of the diamond nitrogen-vacancy center charge state via photoluminescence spectroscopy," 2025.
- [89] S.A. Savinov, V.V. Sychev, and D. Bi, "Diamond nitrogen-vacancy center charge state ratio determination at a given sample point," *Journal of Luminescence*, vol. 248, Aug. 2022, p. 118981.
- [90] M. Fukami, C.G. Yale, P. Andrich, X. Liu, F.J. Heremans, P.F. Nealey, and D.D. Awschalom, "All-Optical Cryogenic Thermometry Based on Nitrogen-Vacancy Centers in Nanodiamonds," *Physical Review Applied*, vol. 12, Jul. 2019, p. 014042.
- [91] E. Fraczek, V.G. Savitski, M. Dale, B.G. Breeze, P. Diggle, M. Markham, A. Bennett, H. Dhillon, M.E. Newton, and A.J. Kemp, "Laser spectroscopy of NV- and NVO colour centres in synthetic diamond," *Optical Materials Express*, vol. 7, Jun. 2017, p. 2571.

Appendix

Appendix A. Abbreviations

PL Photoluminescence

SCDNs Single-crystal diamond needles

CVD Chemical vapor deposition

PE-CVD Plasma-enhanced chemical vapor deposition

HPHT High-pressure high-temperature

ZPL Zero-phonon line

PSB Phonon sideband

PR Phonon replica

NNMF Non-negative matrix factorization

Statement of non-plagiarism

I hereby declare that all information in this report has been obtained and presented in accordance with academic rules and ethical conduct and the work I am submitting in this report, except where I have indicated, is my own work.

Declaration on the use of generative AI tools

I hereby declare that I have used AI tools responsibly and transparently in the preparation of this thesis.

The following AI tools were employed:

- Grammarly AI for grammar refinement and text polishing;
- MATLAB Copilot for code debugging and template scripts generation to support data analysis, which were subsequently verified, modified, and validated by me.

No generative AI-based tool was used to produce raw research results, data analysis conclusions, or original scientific interpretations. All experimental work, data interpretation, and final responsibility for the scientific content remain entirely my own.

Supervisor approval

I, the undersigned, Sergei Malykhin, supervisor of Elena Filonenko, student of the PSRS EMJMD, during her master thesis at University of Eastern Finland certify that I approve the content of this master thesis report entitled "Color centers in diamond needles for all-optical sensing".

25.08.2025, Joensuu

/Sergei Malykhin